



EVALUATION OF THERMAL DIFFUSION COEFFICIENT IN NON-ISOTHERMAL COMPOSITIONAL GRADING SIMULATIONS

Mayra Carvalho de Oliveira Ferreira

Dissertação de Mestrado apresentada ao Programa de Pós-graduação em Engenharia Química, COPPE, da Universidade Federal do Rio de Janeiro, como parte dos requisitos necessários à obtenção do título de Mestre em Engenharia Química.

Orientadores: Frederico Wanderley Tavares
Pedro Henrique Davi Constantino

Rio de Janeiro
Outubro de 2025

EVALUATION OF THERMAL DIFFUSION COEFFICIENT IN
NON-ISOTHERMAL COMPOSITIONAL GRADING SIMULATIONS

Mayra Carvalho de Oliveira Ferreira

DISSERTAÇÃO SUBMETIDA AO CORPO DOCENTE DO INSTITUTO
ALBERTO LUIZ COIMBRA DE PÓS-GRADUAÇÃO E PESQUISA DE
ENGENHARIA DA UNIVERSIDADE FEDERAL DO RIO DE JANEIRO COMO
PARTE DOS REQUISITOS NECESSÁRIOS PARA A OBTENÇÃO DO GRAU
DE MESTRE EM CIÊNCIAS EM ENGENHARIA QUÍMICA.

Orientadores: Frederico Wanderley Tavares
Pedro Henrique Davi Constantino

Aprovada por: Prof. Frederico Wanderley Tavares
Prof. Pedro Henrique Davi Constantino
Ph.D. Marcos Vitor Barbosa Machado
Prof. Pedro Henrique Rodrigues Alijó

RIO DE JANEIRO, RJ – BRASIL
OUTUBRO DE 2025

Ferreira, Mayra Carvalho de Oliveira

Evaluation of Thermal Diffusion Coefficient in Non-Isothermal Compositional Grading Simulations/Mayra Carvalho de Oliveira Ferreira. – Rio de Janeiro: UFRJ/COPPE, 2025.

XVII, 81 p.: il.; 29,7cm.

Orientadores: Frederico Wanderley Tavares

Pedro Henrique Davi Constantino

Dissertação (mestrado) – UFRJ/COPPE/Programa de Engenharia Química, 2025.

Referências Bibliográficas: p. 70 – 74.

1. Thermodiffusion. 2. Compositional Grading. 3. Reservoir Simulation. I. Tavares, Frederico Wanderley *et al.* II. Universidade Federal do Rio de Janeiro, COPPE, Programa de Engenharia Química. III. Título.

Agradecimentos

A realização deste mestrado só foi possível graças ao apoio, incentivo e colaboração de muitas pessoas que estiveram comigo em diferentes momentos desta jornada. A todas elas, deixo aqui meu sincero agradecimento.

Aos meus orientadores Frederico Wanderley Tavares, Rogério Oliveira Espósito e Pedro Henrique Davi Constantino, por todo o apoio no meu desenvolvimento como pesquisadora.

À COPPE/UFRJ e à Petrobras, pela oportunidade de desenvolvimento.

À minha família, por todo carinho e apoio incondicional.

Ao meu esposo, Leandro, pela paciência, apoio e companheirismo constantes, meu porto seguro sempre.

Aos meus filhos, Helena e Ícaro, por entenderem meu tempo de estudo, com a maturidade que a idade lhes permite.

Aos meus colegas da Petrobras, em especial ao Rafael Jesus, pelo incentivo e pela compreensão ao longo desse período.

Resumo da Dissertação apresentada à COPPE/UFRJ como parte dos requisitos necessários para a obtenção do grau de Mestre em Ciências (M.Sc.)

AValiação DO COEFICIENTE DE DIFUSÃO TéRMICA EM SIMULAÇÕES DE GRADAÇÃO COMPOSICIONAL NÃO ISOTéRMICA

Mayra Carvalho de Oliveira Ferreira

Outubro/2025

Orientadores: Frederico Wanderley Tavares
Pedro Henrique Davi Constantino

Programa: Engenharia Química

Esta dissertação analisa como a difusão térmica influencia a gradação composicional em reservatórios de hidrocarbonetos sob condições não isotérmicas. Modelos composicionais convencionais já consideram a segregação gravitacional e a difusão molecular, mas o papel dos gradientes de temperatura, associados ao efeito Soret, ainda não está bem estabelecido na prática da engenharia de reservatórios. Para investigar esse aspecto, diferentes estratégias foram implementadas e testadas em um simulador composicional.

No primeiro conjunto de experimentos, o modelo de Firoozabadi foi modificado para ajustar o parâmetro térmico do CO_2 , avaliando seu impacto em um reservatório predominantemente gasoso com alta concentração desse componente. No segundo conjunto, o modelo de Montel foi adaptado para permitir um parâmetro ajustável por pseudocomponente, aplicando essa formulação a três casos: um cenário sintético do Mar do Norte, um reservatório real da Bacia de Campos e outro da Bacia de Santos, caracterizado por gradientes composicionais mais acentuados.

Os resultados mostraram que, em ambos os conjuntos de experimentos, os modelos modificados produziram ajustes mais próximos aos perfis composicionais medidos em comparação às versões originais, reduzindo os desvios em 20–40 % com base no erro quadrático médio. Essas melhorias foram consistentes entre os casos analisados, indicando que as adaptações podem melhorar a representação dos efeitos de difusão térmica nas condições avaliadas. Embora sejam necessários estudos adicionais para generalizar esses resultados, eles indicam que as abordagens propostas podem orientar futuros aprimoramentos em modelos de gradação composicional não isotérmica.

Abstract of Dissertation presented to COPPE/UFRJ as a partial fulfillment of the requirements for the degree of Master of Science (M.Sc.)

EVALUATION OF THERMAL DIFFUSION COEFFICIENT IN NON-ISOTHERMAL COMPOSITIONAL GRADING SIMULATIONS

Mayra Carvalho de Oliveira Ferreira

October/2025

Advisors: Frederico Wanderley Tavares

Pedro Henrique Davi Constantino

Department: Chemical Engineering

This dissertation examines how thermal diffusion influences compositional grading in hydrocarbon reservoirs under non-isothermal conditions. Conventional compositional models already consider gravitational segregation and molecular diffusion, but the role of temperature gradients, associated with the Soret effect, is still not well established in reservoir engineering practice. To explore this aspect, different strategies were implemented and tested in a compositional simulator.

In the first set of experiments, Firoozabadi's model was modified to adjust the thermal parameter of CO_2 , assessing its impact in a predominantly gas reservoir with a high concentration of this component. In the second set, Montel's model was adapted to allow an adjustable parameter for each pseudo-component, applying this formulation to three cases: a synthetic North Sea scenario, a real Campos Basin reservoir, and another from Santos Basin, characterized by stronger compositional gradients.

Results showed that, in both sets of experiments, the modified models produced a closer match to measured compositional profiles than their original versions, reducing deviations by 20-40 % based on root-mean-square error. These improvements were consistent across all cases, indicating that the proposed adaptations may enhance the representation of thermal-diffusion effects under the examined conditions. Although further study is required to generalize these findings, the results suggest that the approaches explored here may help guide future improvements in non-isothermal compositional-grading models.

Contents

List of Figures	ix
List of Tables	xi
List of Symbols	xiii
List of Abbreviations	xvii
1 Introduction	1
1.1 Motivation	1
1.2 Research Objectives and Scope	2
2 Theoretical Background	5
2.1 Overview of Reservoir Fluid Data and Modeling Workflow	5
2.2 Data Acquisition	5
2.3 PVT Characterization of Reservoir Fluids	7
2.3.1 Constant Composition Expansion Test (CCE)	8
2.3.2 Flash Expansion Test	8
2.3.3 Differential Liberation Test	8
2.3.4 Chromatographic Analysis	8
2.4 Expansion of Heavy Fractions Using Shibata's Quadrature Method	10
2.4.1 Mathematical Derivation of Shibata's Quadrature	10
2.4.2 Application of Shibata's Quadrature	12
2.5 Lumping and EOS Tuning	13
2.6 Compositional Grading in Reservoir Fluids	14
2.7 Classical Thermodynamic Framework	16
2.8 Nonisothermal Reservoirs and Irreversible Thermodynamics	18
2.8.1 Entropy Balance and Production	18
2.8.2 Linear Phenomenological Laws and Onsager Relations	20
3 Literature Review on Multicomponent Thermal Diffusion	24
3.1 Firoozabadi's Model	24

3.2	Espósito et al. correlation	26
3.3	Pedersen’s Model	27
3.4	Montel’s Model	28
3.4.1	Derivations from Montel’s Model	29
4	Methodology	31
4.1	Compositional Reservoir Simulator	31
4.2	Parameter regression of τ_{CO_2} for depth-dependent compositional grading	34
4.2.1	Simulation Setup	35
4.2.2	Fluid Description	36
4.2.3	Optimization Strategy	36
4.3	Parameter Regression for the Montel’s Modified Thermal Diffusion Model	39
4.3.1	Simulation setup	39
4.3.2	Fluid description	40
4.3.3	Optimization strategy	45
5	Results and Discussion	48
5.1	Results of Parameter Regression for τ_{CO_2}	48
5.1.1	Discussion	55
5.2	Results for Montel’s Modified Thermal Diffusion Model	58
5.2.1	Field A	58
5.2.2	Field B	61
5.2.3	Field C	63
5.2.4	Discussion	65
6	Conclusion	68
	References	70
A	Detailed Entropy Balance Derivation	75
B	Detailed Derivation of Linear Phenomenological Laws	79

List of Figures

2.1	Approximation of the heavy-end distribution using pseudocomponents selected from a bounded Gauss-Laguerre quadrature with $\Delta = 2.4$.	13
2.2	Vertical distribution of methane in fluid samples from two wells in the same reservoir.	15
4.1	Optimization loop integrating experimental data, the Python-based optimizer, and the compositional reservoir simulator.	36
5.1	Simulated CO ₂ profiles for fixed τ_{CO_2} values in the range of 0.1 to 2.0.	49
5.2	Simulated CO ₂ profiles for fixed τ_{CO_2} values in the reduced range closer to the optimized value.	49
5.3	Comparison between correlation-based τ_{CO_2} (PSO optimized) and selected fixed-value simulations.	50
5.4	Comparison between CO ₂ mole fraction profiles obtained with the PSO-optimized correlation with Powell refinement.	51
5.5	Comparison between experimental and simulated CH ₄ mole fraction profiles for the PSO optimized correlation and the best fixed value case ($\tau_{\text{CO}_2} = 0.1$).	52
5.6	Comparison between experimental and simulated C ₂₀₊ mole fraction profiles for the PSO optimized correlation and the best fixed value case ($\tau_{\text{CO}_2} = 0.1$).	53
5.7	CO ₂ mole fraction profiles using fixed values $\tau_{\text{CO}_2} = 0.6696$ and $\tau_{\text{CO}_2} = 0.0679$.	54
5.8	CO ₂ mole fraction profiles using fixed values $\tau_{\text{CO}_2} = 0.1262$ and $\tau_{\text{CO}_2} = 0.1591$.	54
5.9	Simulated mole fraction profiles for N ₂ -C ₁ in Field A using Montel's modified thermal diffusion formulation, compared with alternative models.	59

5.10	Simulated mole fraction profiles for CO ₂ in Field A using Montel's modified thermal diffusion formulation, compared with alternative models.	59
5.11	Simulated mole fraction profiles for CN1 in Field A using Montel's modified thermal diffusion formulation, compared with alternative models.	60
5.12	Simulated mole fraction profiles for CN2 in Field A using Montel's modified thermal diffusion formulation, compared with alternative models.	60
5.13	Simulated and measured mole fraction profiles for N ₂ -C ₁ in Field B using Montel's modified thermal diffusion formulation, compared with alternative models.	62
5.14	Simulated and measured mole fraction profiles for C ₂₀₊ in Field B using Montel's modified thermal diffusion formulation, compared with alternative models.	62
5.15	Simulated and measured mole fraction profiles for N ₂ -C ₁ in Field C using Montel's modified thermal diffusion formulation, compared with alternative models.	64
5.16	Simulated and measured mole fraction profiles for C ₂₀₊ in Field C using Montel's modified thermal diffusion formulation, compared with alternative models.	64

List of Tables

2.1	Gauss-Laguerre quadrature values for $n = 3$ and $\Delta = 2.4$	12
2.2	Pseudocomponent characterization for C_{20+} expansion using Shibata's method (bounded Laguerre, $\Delta = 2.4$)	13
4.1	Mole fractions and thermodynamic properties of pseudocomponents at the reference depth (108 m).	37
4.2	Binary interaction coefficients for the adjusted fluid at the reference depth (108 m).	37
4.3	Pseudocomponent compositions for the remaining five PVT samples at different depths.	38
4.4	Configuration of the Particle Swarm Optimization algorithm used for parameter regression.	39
4.5	Thermodynamic properties of pseudocomponents used to describe the oil of Field A.	41
4.6	Matrix of binary interaction parameters (k_{ij}) for Field A.	41
4.7	Depth and mole fraction of component N_2-C_1 for isothermal and non-isothermal cases of Field A.	42
4.8	Depth and mole fraction of component CO_2 for isothermal and non-isothermal cases of Field A.	42
4.9	Depth and mole fraction of component CN1 for isothermal and non-isothermal cases of Field A.	43
4.10	Depth and mole fraction of component CN2 for isothermal and non-isothermal cases of Field A.	43
4.11	Mole fraction of the pseudocomponents for Field B.	44
4.12	Thermodynamic properties of pseudocomponents for Field B	44
4.13	Values of binary interaction coefficients for Field B	45
4.14	Mole fraction of the pseudocomponents for Well 1 in Field C.	46
4.15	Thermodynamic properties of pseudocomponents for Field C.	46
4.16	Values of binary interaction coefficients for Field C	47
4.17	Composition of the pseudocomponents for Wells 2 and 3 in Field C.	47

5.1	τ_{CO_2} values from the PSO-optimized correlation at experimental depths	50
5.2	Comparison of PSO and PSO plus Powell optimization results for the τ_{CO_2} correlation.	51
5.3	Root-mean-square error (RMSE) between simulated and experimental CO_2 mole fractions for different τ_{CO_2} definitions.	52
5.4	RMSE comparison for the optimized correlation and selected fixed τ_{CO_2} values.	55
5.5	Transport coefficients L_i fitted for Field A.	61
5.6	RMSE values for Field A considering each thermal diffusion formulation. 61	
5.7	Optimized L_i values for each pseudocomponent in Field B using Montel's modified thermal diffusion formulation.	63
5.8	RMSE values for Field B considering each thermal diffusion formulation. 63	
5.9	Optimized L_i values for each pseudocomponent in Field C.	65
5.10	RMSE values for Field C considering each thermal diffusion formulation. 65	

List of Symbols

B_g	Gas formation volume factor [$\text{m}^3 \cdot \text{std m}^{-3}$]	8
B_o	Oil formation volume factor [$\text{m}^3 \cdot \text{std m}^{-3}$]	8
C	Normalization constant	10
D	Decay constant	10
D	Molecular diffusion coefficient [$\text{m}^2 \cdot \text{s}^{-1}$]	22
D^P	Pressure diffusion coefficient [$\text{m}^2 \cdot \text{s}^{-1} \cdot \text{Pa}^{-1}$]	22
D^T	Thermal diffusion coefficient [$\text{m}^2 \cdot \text{s}^{-1} \cdot \text{K}^{-1}$]	22
$F(I)$	Continuous distribution function	10
H_i^{ig}	Ideal-gas enthalpy of component i	27
I	Molecular characterization index	10
I_k	Quadrature nodes	10
L_{ij}	Phenomenological coefficient	20
L_{ik}	Phenomenological coefficient relating mass flux to chemical potential gradient of component k	80
L_{ik}	Phenomenological coefficient relating mass flux to chemical potential gradient of component k	21
L_{iq}	Phenomenological coefficient relating mass flux to temperature gradient	21, 80
L_{qk}	Phenomenological coefficient relating heat flux to chemical potential gradients	21, 80
L_{qq}	Phenomenological coefficient relating heat flux to temperature gradient	21, 80

M	Molar mass [g·mol ⁻¹]	14
P	Pressure [Pa]	16
P_b	Bubble-point pressure [Pa]	8
P_c	Critical pressure [Pa]	14
Q^*	Net heat of transport	25
R	Total number of chemical reactions [-]	19, 76
R	Universal gas constant [J·mol ⁻¹ ·K ⁻¹]	17
R_s	Solution gas-oil ratio [std m ³ ·m ⁻³]	8
S_T	Soret coefficient [-]	22
T	Temperature [K]	16
T_c	Critical temperature [K]	14
V	Molar volume	28
W_k	Weight factors associated with z_k	11
X	Thermodynamic force associated with an irreversible flux	20
ΔU_i^{vap}	Energy of vaporization of pure component i	26
ΔU_i^{vis}	Energy of viscous flow of pure component i	26
$\Delta \bar{U}_i$	Partial molar internal energy of component i	26
α_T	Thermal diffusion factor	25
\bar{H}	Molar enthalpy of the mixture	27
\bar{V}	Partial molar volume [m ³ ·mol ⁻¹]	80
\bar{H}_i	Partial molar enthalpy of component i	27
\bar{H}_i^{res}	Partial molar residual enthalpy of component i	27
Π	Viscous stress tensor [Pa]	19, 76
∇	Gradient operator	18
$\nabla \cdot$	Divergence operator	18

$\nabla \mathbf{v}$	Velocity gradient tensor [s^{-1}]	19, 76
$\dot{\xi}_r$	Rate of progress of reaction r [$\text{mol}\cdot\text{m}^{-3}\cdot\text{s}^{-1}$]	19, 76
\hat{f}_i	Fugacity of component i in the mixture [Pa]	17
κ_T	Isothermal compressibility coefficient [Pa^{-1}]	8
Jac	Jacobian matrix	32
\mathbf{J}_i	Diffusion mass flux of component i [$\text{kg}\cdot\text{m}^{-2}\cdot\text{s}^{-1}$]	19
\mathbf{J}_q	Conductive heat flux [$\text{W}\cdot\text{m}^{-2}$]	19
\mathbf{J}_s	Entropy flux [$\text{W}\cdot\text{m}^{-2}\cdot\text{K}^{-1}$]	18
R	Residual vector in Newton–Raphson	32
g	Gravitational acceleration [$\text{m}\cdot\text{s}^{-2}$]	19, 76
q	Total heat flux	20, 78
v	Bulk velocity vector [$\text{m}\cdot\text{s}^{-1}$]	19
x	Vector of unknowns in Newton–Raphson	32
CH_4	methane	14
CO_2	Carbon dioxide	31
μ	Chemical potential [$\text{J}\cdot\text{mol}^{-1}$]	16
$\nu_{i,r}$	Stoichiometric coefficient of species i in reaction r [-]	19, 76
ω	Acentric factor	14
ϕ	Fugacity coefficient	27
ρ	Mass density [$\text{kg}\cdot\text{m}^{-3}$]	18
ρs	Entropy per unit volume [$\text{J}\cdot\text{m}^{-3}\cdot\text{K}^{-1}$]	18
σ	Entropy generation rate [$\text{W}\cdot\text{m}^{-3}\cdot\text{K}^{-1}$]	18
$\tilde{\mu}$	Chemical potential per unit mass [$\text{J}\cdot\text{kg}^{-1}$]	19
c	Density	22
c_{max}	Upper bound of molecular characterization index range	10

c_{min}	Lower bound of molecular characterization index range	10
f	Fugacity [Pa]	17
g	Gravitational acceleration [$\text{m}\cdot\text{s}^{-2}$]	17
h_i	Partial enthalpy of component i	78
i	Component index	8
k_T	Thermal diffusion ratio	25
n	Number of chemical species [-]	19
n	Number of quadrature points	10
n_i	Number of moles of component i	28
q_i	Partial molar heat of transport of component i	28
s	Specific entropy [$\text{J}\cdot\text{kg}^{-1}\cdot\text{K}^{-1}$]	18
s_i^{res}	Residual entropy	28
u	Specific internal energy [$\text{J}\cdot\text{kg}^{-1}$]	19, 75
v	Specific volume [$\text{m}^3\cdot\text{kg}^{-1}$]	19, 75
w_i	Mass fraction of component i [-]	19, 75
w_k	Weights associated with I_k	10
x	Mole fraction [-]	10
x_{plus}	Total mole fraction of the heavy cut [-]	10
z	Depth [m]	16
z_k	Quadrature nodes	11
C_i	Component with i carbon atoms	8

List of Abbreviations

API	American Petroleum Institute	6
ATOMS	Applied Thermodynamics and Molecular Simulation	31
CCE	Constant Composition Expansion	8
CMG	Computer Modelling Group	14
EoS	Equation of State	5
GOR	Gas-Oil Ratio	6
MWD	Measurement While Drilling	7
NEMD	Non-Equilibrium Molecular Dynamics	40
NR	Newton-Raphson	32
PLT	Production Logging Tool	7
PSO	Particle Swarm Optimization	37
PVT	Pressure-Volume-Temperature	5
RERI	Reservoir Engineering Research Institute	31
RMSE	Root-mean-square error	51
TDFRS	Thermal diffusion forced Rayleigh scattering	22
WFT	Wireline Formation Testing	5

Chapter 1

Introduction

1.1 Motivation

Accurate representation of reservoir fluids is essential in petroleum engineering and remains a challenge for oil-and-gas companies. Strategic decisions related to production system design, performance forecasting, and recovery planning depend on the composition and spatial distribution of hydrocarbons within the reservoir. Thermodynamic models play a central role in fluid characterization and are extensively used in simulation and engineering workflows.

Under subsurface conditions, hydrocarbon composition is rarely uniform. Variations with depth are primarily driven by gravity, thermal diffusion, and natural convection. This phenomenon, known as compositional grading, has been extensively examined in phase-behaviour research (DAKE, 1978; ESPÓSITO *et al.*, 2017; FIROOZABADI, 1999; WHITSON and BRULÉ, 2000).

When gravity alone acts upon the system and the reservoir is assumed to be isothermal, the fluid column can be described as being in thermodynamic equilibrium. Heavier components tend to accumulate near the base, while lighter molecules concentrate at the top. This behaviour is well captured by gravity-modified isofugacity equations, as described by WHITSON and BRULÉ (2000).

However, no reservoir is truly at equilibrium. Due to continuous heat flux from the Earth's interior, entropy generation in petroleum reservoirs is an ongoing process. Thermal diffusion, or Soret effect (SORET, 1879 apud DE GROOT and MAZUR, 1984), may either enhance or oppose the compositional grading predicted under isothermal assumptions.

The framework of irreversible thermodynamics, developed by DE GROOT and MAZUR (1984), provides the basis for modeling entropy generation by considering mass and energy transport under non-equilibrium conditions. In this framework, compositional grading is produced by mass fluxes primarily induced by chem-

ical potential gradients, but also influenced by cross-effects associated with temperature and pressure gradients, as described by the Onsager reciprocal relations (DE GROOT and MAZUR, 1984).

While this theoretical framework is well established, its application in practical reservoir simulation remains limited. Thermal diffusion is generally not considered in commercial reservoir simulators, even in those that support compositional modeling. Most tools account for gravity and molecular diffusion, but they usually ignore cross-effects like the Soret effect. This is partly because there isn't much experimental data on multicomponent thermal diffusion behavior under reservoir conditions. These systems usually involve high pressure, high temperature, and many interacting components. In addition, estimating thermal diffusion coefficients is not straightforward, since they depend on composition, temperature, and pressure, and are rarely available for real reservoir fluids.

This dissertation explores this topic by testing existing thermal diffusion models and proposing modifications to improve their ability to reproduce compositional data under non-isothermal conditions. The goal is to evaluate whether these changes lead to more accurate descriptions of compositional grading in systems affected by temperature gradients, compared to standard versions of the models.

1.2 Research Objectives and Scope

This dissertation investigates how thermal diffusion affects compositional grading in hydrocarbon reservoirs under non-isothermal conditions. The main goal is to evaluate existing models for thermal diffusion and test modified versions of these models to see whether they can better reproduce measured compositional profiles from real fluids.

To do this, an existing compositional simulator was adapted to include selected thermal diffusion models. The code calculates one-dimensional composition and pressure profiles by solving the coupled transport equations at steady state, starting from a reference sampling depth. The results are then compared with fluid composition data measured at other depths to check how accurate each model is.

Four models are tested in this study. The first is a semi-empirical correlation originally proposed by DOUGHERTY JR. and DRICKAMER (1955) and later generalized for multiphase systems by FIROOZABADI *et al.* (2000), which includes an adjustable parameter τ . The second, proposed by ESPÓSITO *et al.* (2017), builds on Firoozabadi's formulation by replacing the adjustable τ with a correlation based on fluid properties. The third, from PEDERSEN and LINDELOFF (2003), relates the Heat of Transport to partial molar enthalpies, with ideal-gas heat capacities used as fitting parameters. The fourth is a modified version of the model proposed

by MONTEL *et al.* (2019), which links the Heat of Transport to residual entropy. In this version, the Onsager coefficient is treated as an adjustable parameter, and its performance is compared with the other models to evaluate its potential advantages in representing compositional grading. These models reflect different physical assumptions and offer a comparative basis for evaluation.

In addition to comparing model performance with real fluid data, the study also explores how the presence of contaminants like CO₂ affects compositional grading and thermal transport. One specific case involves fluids with high CO₂ content in the gas zone, where standard models struggle to capture observed profiles. To address this, a modification was proposed and tested for the τ value assigned to CO₂ in Firoozabadi's formulation, aiming to improve the representation of thermal diffusion for this component in such systems.

This study relies on a set of assumptions and boundaries that define its intended scope. The reservoir column is treated as a steady-state system, where compositional variations arise mainly from gravity, molecular diffusion, and thermal diffusion, and convective effects are considered negligible. The PVT samples used for calibration are assumed to be representative of in-situ conditions, and the tuned equation of state is taken as valid throughout the entire column.

The analysis is limited to one-dimensional simulations and to a small number of fluid systems: one reservoir with high CO₂ content used to evaluate the adaptation of Firoozabadi's model, and three additional fluids used in the assessment of the modified Montel formulation, including a synthetic North Sea case, a real Campos Basin reservoir, and a Santos Basin reservoir with stronger compositional gradients. Uncertainties associated with laboratory measurements, heavy-fraction characterization, and pseudocomponent properties may influence the results. Since the proposed modifications were evaluated for a selected set of fluid systems, the conclusions reflect the behavior observed in these cases. Even so, the results highlight the potential for further development and broader evaluation of thermal-diffusion models in different reservoir environments.

Chapter 2 provides the theoretical background on reservoir fluid modeling and introduces the fundamentals of non-equilibrium thermodynamics. Chapter 3 reviews the main models used to describe multicomponent thermal diffusion in hydrocarbon systems. Chapter 4 describes the implementation methodology adopted and the case studies analyzed. Chapter 5 presents the results and provides their interpretation and discussion, and Chapter 6 summarizes the main conclusions and proposes directions for future research.

This dissertation was written with support from ChatGPT (OPENAI), an artificial intelligence language model. The tool was used to assist with grammar revision and consistency of language style. All ideas, reasoning, and conclusions presented

here are the result of the author's work.

Chapter 2

Theoretical Background

Reservoir fluid modeling is a fundamental tool used to describe the phase behavior of hydrocarbons in the subsurface and to support the interpretation of field production performance. This chapter explains how reservoir fluid data are acquired, processed, and used to build compositional models for simulation. It also discusses the assumptions typically made when extending laboratory measurements to reservoir scale applications and introduces the concept of compositional gradients.

2.1 Overview of Reservoir Fluid Data and Modeling Workflow

One of the main challenges in reservoir fluid modeling is extrapolating limited and localized experimental data to describe fluid properties across the entire reservoir and throughout its productive life. This process relies heavily on established Pressure-Volume-Temperature (PVT) analysis methods and tuning procedures applied to an Equation of State (EoS) (DAKE, 1978).

The data required for this purpose are usually obtained during the drilling of the initial exploratory or appraisal wells through downhole fluid sampling procedures (ESPÓSITO *et al.*, 2017; WHITSON and BRULÉ, 2000). These samples are then subjected to laboratorial thermodynamic characterization. The measured properties are extrapolated to other pressure and temperature conditions using an equation of state (EoS), enabling the construction of a compositional model suitable for reservoir simulation.

2.2 Data Acquisition

Formation fluid samples for PVT characterization are typically collected during the early phases of field development, especially when drilling exploratory or ap-

praisal wells. During the drilling phase, fluid samples can be collected using a Wire-line Formation Testing (WFT) tool, which retrieves fluids from selected depths. The collected samples are later analyzed in the laboratory to determine fluid composition and other thermodynamic properties. Alternatively, samples can be obtained from a test separator after the well has been finalized and connected to surface facilities. In this case, the sample reflects the composition of the entire perforated interval (WHITSON and BRULÉ, 2000).

For compositional modeling, pre-production WFT samples are preferred when available, as they provide depth-specific data needed to analyze compositional gradients. At this stage, the reservoir is usually assumed to be in a quasi-static equilibrium state, where convective transport is negligible and no significant chemical reactions or external mass exchange occur after migration (PEDERSEN and LINDELOFF, 2003). This assumption is based on the long geological timescales involved in petroleum systems, often lasting millions of years, which give enough time for diffusion to redistribute the fluid components. In deep and undisturbed reservoirs, the timescale of molecular diffusion is much shorter than the geologic timeframe, which supports the use of equilibrium equations and static profiles to represent compositional grading.

During WFT acquisition, the tool is positioned at the target depth, and the formation fluid is collected in a pressurized sample chamber. Multiple sampling depths may be selected within the same well. A common challenge in this process is contamination by drilling fluid filtrate, which can introduce significant deviations in measured GOR, API gravity, and component concentrations (ROSA *et al.*, 2006). Such alterations may affect not only bulk PVT properties, but also the depth-dependent compositional trends that are critical for analyzing reservoir grading.

To correct for contamination, laboratories typically apply mathematical procedures such as Skimming and Subtraction. The resulting fluid compositions are already adjusted for the estimated contamination level, which is provided for each sample along with other basic acquisition data. Although these corrections are widely used, they do not eliminate all uncertainty. High levels of contamination can reduce the reliability of the compositional data, especially for lighter components, which tend to show more variation during sampling and correction (LOURENÇO *et al.*, 2016).

In this study, the selection of fluid samples followed good practice by favoring those with lower contamination levels when available. In some cases, more than one sample was collected at the same depth, and small differences in composition were observed. These variations are normal and can be caused by several factors, including the timing of collection, lab procedures, or the degree of contamination. WFT samples, in particular, tend to be more affected by contamination because

they are taken during or soon after drilling, when some drilling fluid may still be present in the reservoir. Although the tools include a cleanup stage and the laboratory corrections are applied, some uncertainty remains in the final composition. Surface samples collected from test separators are generally cleaner, since the well has already produced enough to remove most of the filtrate from the invaded zone. These factors help explain why fluid compositions from PVT analyses should be seen as estimates rather than exact values, and why the context of each sample matters when using the data in model calibration.

Despite these uncertainties, PVT data are still the standard reference for fluid characterization in reservoir engineering, mainly because they provide necessary parameters for compositional modeling, such as formation volume factor, bubble point pressure, and viscosity. As WHITSON and BRULÉ (2000) note, their value lies not in delivering exact compositions, but in offering a consistent and technically grounded basis to describe reservoir fluids.

In addition to collecting fluid samples, WFT tools also measure pressure and temperature from the formation at each sampling depth. These measures are highly accurate and are commonly used to build vertical pressure and temperature profiles. Pressure data help define fluid gradients and contacts, while temperature data support the estimation of the local geothermal gradient (SERRA, 2008).

Another useful source of pressure and temperature information is the Production Logging Tool (PLT) or dedicated temperature logs, which are run during production evaluation and provide accurate data for gradient calculations. As with WFT, these tools are not run in every well due to operational and economic constraints.

When WFT or PLT data are not available, basic log profiles can still be used. Conventional wireline logging tools and MWD (Measurement While Drilling) systems include temperature sensors as secondary measurements. While these measures are useful for identifying regional trends, they typically lack the precision required for detailed modeling of reservoir fluid behavior.

2.3 PVT Characterization of Reservoir Fluids

PVT analysis consists of a series of laboratory experiments performed on reservoir fluid samples to determine their thermodynamic properties and chemical composition (ESPÓSITO *et al.*, 2017). These tests provide the basic data needed to build a compositional model and support predictions of fluid behavior under varying pressure and temperature conditions.

In this study, PVT characterization provides the necessary data to calibrate the equation of state, analyze compositional gradients, and evaluate thermal diffusion models. The tests described below are part of the standard workflow used to obtain

this information from the fluid samples collected in the field (ROSA *et al.*, 2006).

2.3.1 Constant Composition Expansion Test (CCE)

In this procedure, the reservoir fluid is placed in a pressurized PVT cell at an initial pressure higher than the reservoir pressure, under isothermal conditions. The pressure is then reduced in steps, without removing the gas that is released. The gas remains in contact with the oil phase, so the overall composition of the system is preserved.

This test is used to determine the bubble-point pressure (P_b) and the isothermal compressibility coefficient (κ_T). If the cell volume allows for full depressurization to standard conditions, it is also possible to determine the two-phase formation volume factor, the solution gas-oil ratio (R_s), and other volumetric properties.

2.3.2 Flash Expansion Test

In this test, the reservoir fluid is abruptly depressurized from an initial pressure higher than the reservoir pressure to standard conditions. The gas is collected in a gasometer, while the liquid phase is weighed using an Erlenmeyer flask. The overall composition of the reservoir fluid system is obtained by mass balance, after chromatographic analysis of both phases. This test also provides key values such as the gas-oil ratio (GOR), API gravity, and isothermal compressibility.

2.3.3 Differential Liberation Test

The differential liberation test involves a multi-stage depressurization sequence, where the pressure is reduced step-by-step below the bubble point, and the gas released at each stage is removed before proceeding. Unlike the flash test, this method isolates the gas at each pressure level, allowing for more detailed analysis.

As a result, the oil formation volume factor (B_o), gas formation volume factor (B_g), and solution gas-oil ratio (R_s) are determined at each stage. This makes the test more representative of how the fluid behaves under reservoir depletion conditions.

2.3.4 Chromatographic Analysis

Chromatographic analysis is used to determine the composition of both the liquid and gas phases obtained during laboratory experiments. After flash separation, the reservoir fluid is split into separator gas and dead oil, which are analyzed separately. The liquid and gas phases are later recombined using the measured GOR to estimate the original live oil composition.

Gas chromatography is used to analyze both the gas and liquid phases of the sample. For gas, the sample is injected directly into the system through a valve. For oil, a small amount of the liquid is injected into a heated chamber, where it is vaporized. In both cases, the sample is carried through a column by an inert gas, usually helium. As it travels, the different components separate depending on how they interact with the inner surface of the column. Lighter substances, with lower boiling points, tend to come out first. As each component reaches the end of the column, it is detected and shown as a peak on the chromatogram, and the area under each peak is proportional to the concentration of that component in the sample (DANESH, 1998).

The result is a list of hydrocarbon components grouped by carbon number, where C_i represents all molecules with i carbon atoms. Components are reported individually up to a cutoff carbon number, and heavier fractions are grouped into a single component referred to as the plus fraction. This fraction is treated as a pseudocomponent, a simplification in which a group of components is represented as a single one, with properties estimated using mixing rules that reflect the overall composition of the group.

The quality of this data depends on several factors, including the performance of the chromatograph, calibration routines, operator experience, and the condition of the sample. Small errors or inconsistencies in this step can directly affect model calibration and the interpretation of compositional gradients, especially for light components and trace species. For example, variations in reported concentrations of N_2 or CO_2 are common, even between samples collected at the same depth, and may affect the model response (WHITSON and BRULÉ, 2000).

A particular challenge comes from the heavy-end fraction. This pseudocomponent represents all hydrocarbons heavier than the last component identified in the chromatographic analysis. Its properties are not measured directly, but instead estimated as the difference needed to close the overall fluid composition. As a result, it tends to accumulate small errors from the measurement of lighter components, making the plus fraction one of the most uncertain parts of the fluid description (WHITSON, 1983).

One way to deal with this uncertainty is to split the plus fraction into pseudocomponents with estimated properties. This approach allows for a better representation of fluid behavior in the model. In this study, the quadrature method proposed by SHIBATA *et al.* (1987) is applied, as described in the next section.

2.4 Expansion of Heavy Fractions Using Shibata’s Quadrature Method

To improve the description of the heavy end in compositional models, a common strategy is to split the plus fraction into multiple pseudocomponents instead of representing it with a single value. This helps capture the variation in properties across the heavy range and gives the model more flexibility to match phase behavior and volumetric data, even when only a limited number of components are measured (WHITSON, 1983).

One approach is to use the quadrature method proposed by SHIBATA *et al.* (1987), which is adopted in this work. In this approach, the heavy fraction is described as a continuous distribution and then divided into a few representative pseudocomponents using Gauss quadrature. A truncated exponential distribution is typically used to better reflect how heavier components behave in real fluids (WHITSON, 1983).

The next section presents the mathematical formulation and shows how the method was applied in this work.

2.4.1 Mathematical Derivation of Shibata’s Quadrature

The quadrature method starts by assuming that the heavy-end components follow a continuous distribution, denoted by $F(I)$, where I is a molecular characterization index such as carbon number or molar mass. The total mole fraction of the plus fraction is the integral of this distribution over a given range:

$$x_{\text{plus}} = \int_{c_{\text{min}}}^{c_{\text{max}}} F(I) dI \quad (2.1)$$

with c_{min} and c_{max} defining the index limits.

The integral in Equation 2.1 is approximated using an n -point Gauss quadrature:

$$\int_{c_{\text{min}}}^{c_{\text{max}}} F(I) dI \approx \sum_{k=1}^n w_k F(I_k) \quad (2.2)$$

where I_k denotes the quadrature points and w_k their associated weights. Each I_k corresponds to a pseudocomponent, while w_k gives the normalized mole fractions.

In many petroleum systems, the distribution $F(I)$ tends to follow an exponential form:

$$F(I) = C e^{-D(I-c_{\text{min}})} \quad (2.3)$$

where D is a decay constant and C is a normalization constant.

For this exponential form, it is convenient to use Gauss-Laguerre quadrature. To apply it, the variable is changed:

$$z = D(I - c_{min}) \quad (2.4)$$

$$I = c_{min} + \frac{z}{D} \quad (2.5)$$

Differentiating and substituting into the integral:

$$dI = \frac{1}{D} dz \quad (2.6)$$

$$\int_{c_{min}}^{c_{max}} C e^{-D(I-c_{min})} dI = C \int_0^{D(c_{max}-c_{min})} e^{-z} \cdot \frac{1}{D} dz \quad (2.7)$$

The integral becomes:

$$\int_{c_{min}}^{c_{max}} F(I) dI = \frac{C}{D} \int_0^{\Delta} e^{-z} dz \quad (2.8)$$

with:

$$\Delta = D(c_{max} - c_{min}) \quad (2.9)$$

This integral can now be approximated with a generalized Gauss-Laguerre quadrature:

$$\int_0^{\Delta} e^{-z} dz \approx \sum_{k=1}^n W_k \quad (2.10)$$

where W_k are the quadrature weights associated with the Laguerre roots z_k .

Thus, the total mole fraction of the continuous heavy cut is written as:

$$x_{\text{plus}} \approx \frac{C}{D} \sum_{k=1}^n W_k \quad (2.11)$$

Solving for the normalization constant C :

$$C = \frac{D \cdot x_{\text{plus}}}{\sum_{k=1}^n W_k} \quad (2.12)$$

Returning to the original variable I , the pseudocomponent indices are obtained from:

$$I_k = c_{min} + \frac{z_k}{D} \quad (2.13)$$

The mole fraction for each pseudocomponent is then:

$$x_k = \frac{C}{D} \cdot W_k = x_{\text{plus}} \cdot \frac{W_k}{\sum_{j=1}^n W_j} \quad (2.14)$$

2.4.2 Application of Shibata's Quadrature

To illustrate the application of the quadrature method derived in subsection 2.4.1, this section presents an example based on the characterization of a C_{20+} fraction with molar mass of $482 \text{ g}\cdot\text{mol}^{-1}$ and mole fraction of 4.73%.

Assuming $D = -0.06$ and $[c_{\min}, c_{\max}] = [20, 60]$, the quadrature is applied using three pseudocomponents.

$$\Delta = |D|(c_{\max} - c_{\min}) = 0.06(60 - 20) = 2.4 \quad (2.15)$$

These values were tabulated by SHIBATA *et al.* (1987) for two and three points, and for Δ values ranging from 1 to infinity.

The pseudocomponent indices are then calculated as:

$$I_k = 20 + \frac{z_k}{0.06} \quad (2.16)$$

and their normalized mole fractions are obtained from:

$$x_k = 0.0473 \cdot \frac{W_k}{\sum W_k} \quad (2.17)$$

To estimate the molar mass of each pseudocomponent, the following empirical correlation by KATZ and FIROOZABADI (1978) is used:

$$M(I_k) = 14I_k - 4 \quad (2.18)$$

The Laguerre roots z_k and weights W_k for $n = 3$ and $\Delta = 2.4$ are shown in Table 2.1, and the resulting pseudocomponents appear in Table 2.2. Their selection within the continuous distribution, shown in Figure 2.1, provide a more detailed representation of the fluid's heavy-end for reservoir modeling purposes.

Table 2.1: Gauss-Laguerre quadrature values for $n = 3$ and $\Delta = 2.4$

z_k	W_k
0.2025	0.4607
0.9983	0.4142
2.0286	0.1251

Table 2.2: Pseudocomponent characterization for C_{20+} expansion using Shibata’s method (bounded Laguerre, $\Delta = 2.4$)

Pseudocomponent	Carbon Number	Molar Mass ($\text{g}\cdot\text{mol}^{-1}$)	Mole Fraction (%)
C23	23.38	323.25	2.18
C37	36.64	508.93	1.96
C54	53.81	749.34	0.59

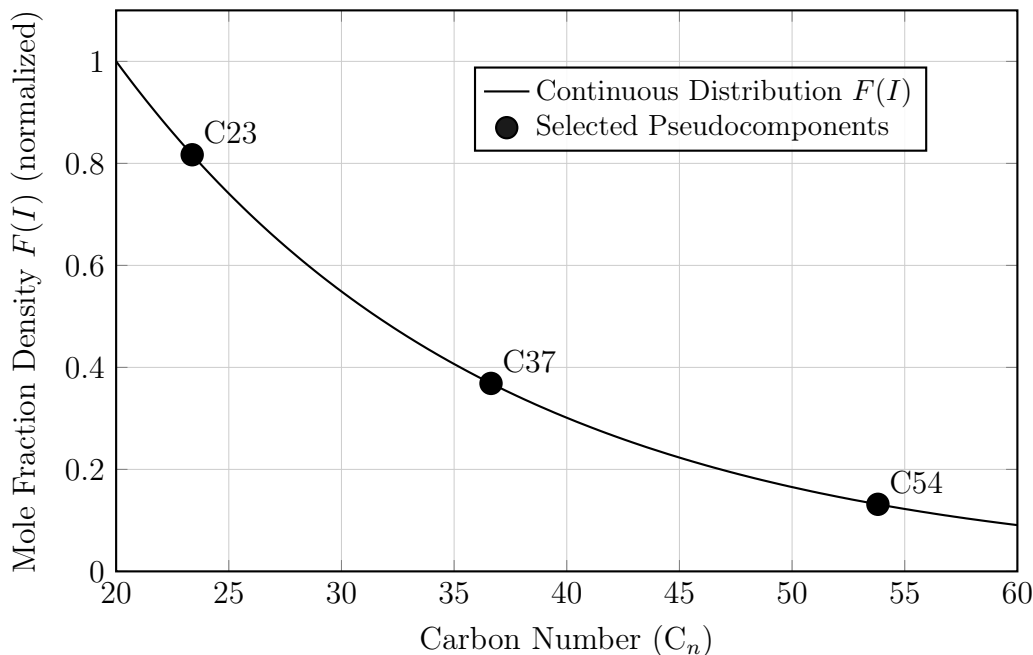


Figure 2.1: Approximation of the heavy-end distribution using pseudocomponents selected from a bounded Gauss-Laguerre quadrature with $\Delta = 2.4$.

2.5 Lumping and EOS Tuning

After the fluid composition is defined, the next step is to prepare the data for use in reservoir simulation.

The full composition obtained from laboratory analysis and the mathematical treatment of the heavy-end usually contains a large number of components. Using all of them in a compositional simulator can lead to high computational cost and convergence issues. To reduce complexity while preserving the fluid behavior, similar components are grouped into a smaller number of pseudocomponents, a process known as lumping.

Component grouping is typically based on similarity in properties such as molar mass, critical conditions, or boiling range. The idea is to reduce the number of components while keeping the overall fluid behavior as close as possible to the

original, either by preserving the shape of the phase envelope or minimizing average deviations in thermodynamic properties.

Once lumped, the thermodynamic properties of the new components are calibrated by adjusting the parameters of the chosen equation of state. The tuning process typically involves modifying critical properties and binary interaction coefficients to match the experimental PVT data.

After tuning, each pseudocomponent is assigned a set of thermodynamic properties, such as molar mass (M), critical pressure (P_c), critical temperature (T_c), acentric factor (ω), and volume-shift term used in the Peneloux correction. These values can be estimated using mixing rules, empirical correlations, or existing component libraries.

In this study, these steps are performed using WinProp version 2022.10, a compositional fluid characterization tool developed by CMG (COMPUTER MODELLING GROUP LTD., 2022). WinProp allows input of laboratory data, application of lumping strategies, EoS selection and tuning, and generation of fluid property tables for use in simulation. Other commercial tools with similar functionality are also widely used in the industry.

Although WinProp was selected for this work, other commercial PVT and fluid-modeling tools are also commonly used in reservoir engineering. Among them, PVT-Sim stands out as an established platform for fluid characterization and equation-of-state regression, and is frequently employed in industry workflows (CALSEP A/S, 2022).

2.6 Compositional Grading in Reservoir Fluids

PVT data from fluid samples collected at different depths often reveal systematic trends in hydrocarbon composition. An example is shown in Figure 2.2, which displays the vertical distribution of methane (CH_4) in two wells from the same accumulation. In Well 1, three samples were collected at distinct depths, while Well 2 provided a single data point. The measurements were obtained from internal PVT reports provided by Petrobras ¹, following the analysis workflow described in Section 2.3. The x-axis shows the methane mole percentage, and the y-axis represents the relative depth, referenced to an arbitrary origin for visualization purposes. In this example, a decreasing trend in methane concentration is observed with depth.

¹Information supplied by PETROBRAS. Internal PVT reports, direct communication, 2025.

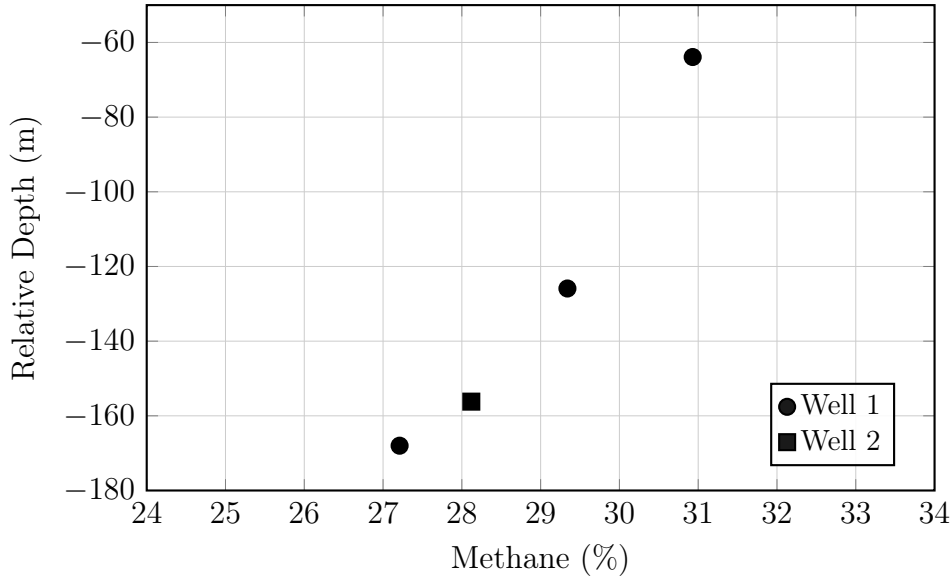


Figure 2.2: Vertical distribution of methane in fluid samples from two wells in the same reservoir.

The variation reflects a pattern that has been widely documented in petroleum systems. This behavior is referred to as compositional grading and describes the gradual variation in fluid composition along the reservoir column. The topic has been extensively studied in the context of phase behavior and thermodynamic modeling of subsurface fluids (ESPÓSITO *et al.*, 2017; FIROOZABADI, 1999; WHITSON and BRULÉ, 2000).

Several physical and geological mechanisms contribute to compositional grading in petroleum reservoirs. One of the most relevant is gravitational segregation, which causes heavier components, such as long-chain hydrocarbons and aromatics, to concentrate at deeper portions of the reservoir, while lighter molecules like methane and ethane accumulate near the top. This effect becomes more significant in reservoirs with large vertical extension (CREEK and SCHRADER, 1985; ESPÓSITO *et al.*, 2017; LIRA-GALEANA *et al.*, 1994; MONTEL and GOUEL, 1985; OKOH *et al.*, 2020; SCHULTE, 1980; WHEATON, 1991; WHITSON and BRULÉ, 2000).

Thermal gradients also play an important role. As temperature typically increases with depth, thermal diffusion (also referred to as the Soret effect) may cause lighter components to migrate downward and heavier ones to move upward, modifying the distribution expected from gravitational segregation. The resulting compositional profile is governed by the balance between gravitational and thermal effects (BAGHOOEE *et al.*, 2021; DOUGHERTY JR. and DRICKAMER, 1955; ESPÓSITO *et al.*, 2017; FIROOZABADI, 1999; FIROOZABADI *et al.*, 2000; GHORAYEB and FIROOZABADI, 2000a; MONTEL *et al.*, 2019; PEDERSEN and LINDELOFF, 2003; SHAIKH *et al.*, 2024; VINHAL *et al.*, 2021).

In some cases, reservoir compartmentalization can influence the observed gradi-

ent. Structural and stratigraphic barriers such as faults, shale layers, or diagenetic seals may restrict vertical and lateral fluid communication. These discontinuities can interrupt the natural redistribution of components, leading to variations that deviate from continuous equilibrium profiles (DONG *et al.*, 2007; GO *et al.*, 2012; SMALLEY and ENGLAND, 1994).

Compositional differences may also be related to the migration history of hydrocarbons. During migration, lighter components tend to partition into the gas phase, while heavier fractions remain behind. This process can produce a stratified composition that reflects transport effects rather than local thermodynamic equilibrium at the trap (ENGLAND *et al.*, 1987; PETERS and FOWLER, 2002; THOMPSON, 1987).

In addition, natural convection may develop in reservoirs with high permeability and significant temperature gradients. These convective flows transport components through the reservoir, modifying the gradients expected from molecular diffusion. The extent of this effect depends on the reservoir's geometry and the intensity of convective movement, which can either enhance or reduce compositional variation (GHORAYEB and FIROOZABADI, 2000b; RILEY and FIROOZABADI, 1998).

Compositional grading arises from several interacting effects and can produce complex profiles along the reservoir column. Laboratory measurements, such as PVT reports, help to identify these variations, but they usually cover only a limited number of wells or depths. To understand how fluids behave beyond the sampled intervals, or under conditions different from those measured, it is necessary to use thermodynamic models. These models extrapolate the available information, support predictions in areas without samples, and allow the evaluation of fluid behavior under varying temperature, pressure, and compositions, providing a consistent framework to represent the combined effects of gravity, thermal diffusion, and other mechanisms. The next section introduces the theoretical background for this approach, starting with the classical treatment of isothermal systems.

2.7 Classical Thermodynamic Framework

Many reservoirs can be treated as isothermal systems. In such cases, classical thermodynamics provides the basis for describing the variation of composition with depth. Under equilibrium conditions, the chemical potential of each component is uniform throughout the system. This condition applies only when external fields are absent.

$$\mu_i(P, T, x_1, x_2, \dots, x_n) = \text{constant} \quad (2.19)$$

where μ_i is the chemical potential of component i at a given pressure P , temperature T , and mole fraction of components x_i .

When external fields act on the system, their contribution is added to the chemical potential so that the total potential remains constant:

$$\mu_i^{\text{tot}} = \mu_i + \mu_i^{\text{field}} = \text{constant} \quad (2.20)$$

In hydrocarbon reservoirs, gravity is the main external field, and its contribution is:

$$\mu_i^{\text{grav}}(z) = M_i g z \quad (2.21)$$

where M_i is the molar mass of component i , g is the gravitational acceleration, and z is the depth.

At equilibrium, the total potential at depth z is equal to that at the reference depth z_{ref} :

$$\mu_i^{\text{tot}}(z) = \mu_i^{\text{tot}}(z_{\text{ref}}) \quad (2.22)$$

$$\mu_i(z) + M_i g z = \mu_i(z_{\text{ref}}) + M_i g z_{\text{ref}} \quad (2.23)$$

Rearranging leads to:

$$\mu_i(z) - \mu_i(z_{\text{ref}}) = -M_i g (z - z_{\text{ref}}) \quad (2.24)$$

The chemical potential is related to fugacity by:

$$\mu_i(z) = \mu_i(z_{\text{ref}}) + RT \ln \left[\frac{\hat{f}_i(z)}{\hat{f}_i(z_{\text{ref}})} \right] \quad (2.25)$$

Substituting Equation 2.24 into Equation 2.25:

$$RT \ln \left[\frac{\hat{f}_i(z)}{\hat{f}_i(z_{\text{ref}})} \right] = -M_i g (z - z_{\text{ref}}) \quad (2.26)$$

$$\ln \left[\frac{\hat{f}_i(z)}{\hat{f}_i(z_{\text{ref}})} \right] = -\frac{M_i g (z - z_{\text{ref}})}{RT} \quad (2.27)$$

Exponentiating both sides yields:

$$\frac{\hat{f}_i(z)}{\hat{f}_i(z_{\text{ref}})} = \exp \left[-\frac{M_i g (z - z_{\text{ref}})}{RT} \right] \quad (2.28)$$

From these relations, the gravity-corrected fugacity equation becomes:

$$\hat{f}_i(z) = \hat{f}_i(z_{\text{ref}}) \exp \left[-\frac{M_i g (z - z_{\text{ref}})}{RT} \right] \quad (2.29)$$

Equation 2.29 describes the change in fugacity of each component i with depth in an isothermal system. The exponential term shows that gravity has a stronger effect on heavier components, which tend to accumulate at greater depths, while lighter ones concentrate near the top. This expression is the starting point for predicting vertical compositional gradients in isothermal reservoirs (ESPÓSITO *et al.*, 2017; WHITSON and BRULÉ, 2000).

2.8 Nonisothermal Reservoirs and Irreversible Thermodynamics

Gravity alone does not account for the compositional gradients observed in many reservoirs (ESPÓSITO *et al.*, 2017; MONTEL and GOUEL, 1985). A geothermal gradient is always present and produces a continuous heat flux from deeper to shallower layers. This flux generates entropy and introduces irreversibility into the system. In cases where the thermal contribution plays a secondary role, the classical isothermal framework can still provide a good approximation. When temperature effects cannot be neglected, however, a nonisothermal description becomes necessary to represent the observed compositional behavior.

In such systems, entropy is generated continuously by irreversible processes, and the reservoir does not reach global equilibrium. Irreversible thermodynamics provides the basis to describe these conditions, relying on the local equilibrium hypothesis. This principle assumes that each infinitesimal element behaves as if it were in equilibrium, so intensive variables such as temperature, pressure, and chemical potential remain uniform within that element (DE GROOT and MAZUR, 1984; FIROOZABADI, 1999).

2.8.1 Entropy Balance and Production

A central principle of irreversible thermodynamics is the non-negativity of entropy production. According to the second law of thermodynamics, any spontaneous process in a closed system proceeds in the direction of increasing the total entropy, considering the system and its surroundings. This idea is expressed locally through the entropy balance, where entropy changes arise from both transport across system boundaries and internal generation by irreversible processes.

The local entropy balance is expressed as:

$$\frac{\partial(\rho s)}{\partial t} + \nabla \cdot \mathbf{J}_s = \sigma \quad (2.30)$$

$$\sigma \geq 0 \quad (2.31)$$

where ρ is the mass density, s is the specific entropy, ρs is the entropy per unit volume, \mathbf{J}_s is the entropy flux, and σ is the entropy generation rate.

Following FIROOZABADI (1999), the entropy flux in porous media includes contributions from bulk convection, conductive heat transfer, and multicomponent diffusion:

$$\mathbf{J}_s = \rho s \mathbf{v} + \frac{\mathbf{J}_q}{T} - \sum_{i=1}^n \frac{\tilde{\mu}_i}{T} \mathbf{J}_i \quad (2.32)$$

where \mathbf{v} is the bulk velocity vector, \mathbf{J}_q is the conductive heat flux, \mathbf{J}_i is the diffusion mass flux of component i , n is the number of chemical species, and $\tilde{\mu}_i$ is the chemical potential per unit mass.

Under the local equilibrium hypothesis, the Gibbs relation applies within each infinitesimal element in terms of specific properties:

$$T ds = du + P dv - \sum_{i=1}^n \tilde{\mu}_i dw_i \quad (2.33)$$

where s is the specific entropy, u is the specific internal energy, $v = \rho^{-1}$ is the specific volume, and w_i is the mass fraction of component i .

Combining the Gibbs relation with the local energy and species balances, written in the classical form of non-equilibrium thermodynamics (DE GROOT and MAZUR, 1984),

$$\rho \frac{du}{dt} = -\nabla \cdot \mathbf{J}_q - P(\nabla \cdot \mathbf{v}) - \mathbf{\Pi} : \nabla \mathbf{v} + \sum_{i=1}^n \mathbf{J}_i \cdot \mathbf{F}_i \quad (2.34)$$

$$\rho \frac{dw_i}{dt} = -\nabla \cdot \mathbf{J}_i + \sum_{r=1}^R \nu_{i,r} \dot{\xi}_r \quad (2.35)$$

where $\mathbf{\Pi}$ is the viscous stress tensor, $\nabla \mathbf{v}$ is the velocity gradient tensor, \mathbf{F}_i is the external force per unit mass acting on species i (such as gravitational or electrical), $\nu_{i,r}$ is the stoichiometric coefficient of species i in reaction r , $\dot{\xi}_r$ is the rate of progress of reaction r , and R is the total number of chemical reactions.

Inserting Equation 2.34 and Equation 2.35 into these relations into the Gibbs relation leads to the local expression for entropy production:

$$\begin{aligned} \sigma = & -\frac{1}{T^2} \left(\mathbf{J}_q - \sum_{i=1}^n \mathbf{J}_i h_i \right) \cdot \nabla T - \frac{1}{T} \sum_{i=1}^n \mathbf{J}_i \cdot [\nabla_T(\tilde{\mu}_i) - \mathbf{g}] \\ & - \frac{1}{T} (\boldsymbol{\Pi} : \nabla \mathbf{v}) + \frac{1}{T} \sum_{r=1}^R \mathcal{A}_r \dot{\xi}_r, \end{aligned} \quad (2.36)$$

where h_i is the partial enthalpy of component i , \mathbf{g} is the gravitational acceleration, and \mathcal{A}_r is the chemical affinity of reaction r .

It is convenient to introduce the total heat flux,

$$\mathbf{q} = \mathbf{J}_q - \sum_{i=1}^n \mathbf{J}_i h_i \quad (2.37)$$

which combines conductive and diffusive contributions.

In this form, the entropy production naturally separates into flux–force pairs, forming the basis for the linear phenomenological relations discussed in the next subsection.

A detailed derivation of Equation 2.36 from Equation 2.30 and Equation 2.32 is presented in Appendix A, following the treatments in DE GROOT and MAZUR (1984) and FIROOZABADI (1999).

2.8.2 Linear Phenomenological Laws and Onsager Relations

As explained by DE GROOT and MAZUR (1984), for systems close to thermodynamic equilibrium, irreversible fluxes are linearly proportional to the corresponding thermodynamic forces. These linear relations are known as phenomenological equations and are written as:

$$\mathbf{J}_i = \sum_j \mathbf{L}_{ij} \mathbf{X}_j \quad (2.38)$$

where \mathbf{J}_i denotes an irreversible flux and \mathbf{X}_j its conjugate force.

In this notation, the entropy production density is expressed as:

$$\sigma = \sum_i \mathbf{J}_i \cdot \mathbf{X}_i \quad (2.39)$$

Substituting Equation 2.38 into Equation 2.39, gives:

$$\sigma = \sum_{ij} L_{ij} \mathbf{X}_i \cdot \mathbf{X}_j \quad (2.40)$$

where L_{ij} are the scalar phenomenological coefficients.

According to the Curie principle, coupling between fluxes and forces occurs only when they have the same tensorial order and compatible symmetry, and the corresponding coefficient vanishes otherwise (DE GROOT and MAZUR, 1984). Under suitable symmetry conditions and microscopic reversibility, the Onsager reciprocal relations hold:

$$L_{ij} = L_{ji} \quad (2.41)$$

For a multicomponent petroleum reservoir subject to mass, heat, and gravitational segregation, the relevant irreversible fluxes are the total heat flux \mathbf{q} and the $n - 1$ independent mass diffusion fluxes \mathbf{J}_i . Using the constraint $\sum_{i=1}^n \mathbf{J}_i = 0$, the entropy production in Equation 2.36 can be rewritten in terms of these independent fluxes and their associated forces. The resulting phenomenological laws are conveniently expressed in matrix form:

$$\begin{bmatrix} \mathbf{q} \\ \mathbf{J}_1 \\ \vdots \\ \mathbf{J}_{n-1} \end{bmatrix} = \begin{bmatrix} L_{qq} & L_{q1} & \cdots & L_{q,n-1} \\ L_{1q} & L_{11} & \cdots & L_{1,n-1} \\ \vdots & \vdots & \ddots & \vdots \\ L_{n-1,q} & L_{n-1,1} & \cdots & L_{n-1,n-1} \end{bmatrix} \begin{bmatrix} X_q \\ X_1 \\ \vdots \\ X_{n-1} \end{bmatrix} \quad (2.42)$$

where \mathbf{q} is the total heat flux vector, \mathbf{J}_i is the mass diffusion flux of component i , $X_q = -\nabla T/T^2$ is the thermal driving force, and

$$X_i = -\frac{1}{T} [\nabla_T(\tilde{\mu}_i) - \nabla_T(\tilde{\mu}_n)]$$

are the combined contributions of chemical potential and gravitational acceleration.

The corresponding expressions for the heat flux and the i -th mass diffusion flux are:

$$\mathbf{q} = -\frac{L_{qq}}{T^2} \nabla T + \sum_{k=1}^{n-1} L_{qk} \left[-\frac{1}{T} \nabla_T(\tilde{\mu}_k - \tilde{\mu}_n) \right] \quad (2.43)$$

$$\mathbf{J}_i = -\frac{L_{iq}}{T^2} \nabla T + \sum_{k=1}^{n-1} L_{ik} \left[-\frac{1}{T} \nabla_T(\tilde{\mu}_k - \tilde{\mu}_n) \right] \quad (2.44)$$

These expressions illustrate the Curie principle, only flux–force pairs of the same tensorial order contribute to cross effects. In Equation 2.43, the direct term proportional to ∇T corresponds to Fourier’s law, while the cross term represents the Dufour effect, that is, a heat flux induced by composition gradients. In Equation 2.44, the coefficients L_{ik} describe molecular diffusion, whereas the term proportional to L_{iq} represents the Soret, or thermal diffusion, contribution to mass transport (FIROOZ-ABADI, 2016).

By expanding the chemical potential difference in composition and pressure, the diffusion laws can be written in terms of molecular, thermal, and pressure diffusion coefficients. These contributions can be grouped into the compact matrix form

$$\mathbf{J} = -c (\mathbf{D} \cdot \nabla \mathbf{x} + \mathbf{D}^T \nabla T + \mathbf{D}^P \nabla P) \quad (2.45)$$

where c is the density, \mathbf{D} , \mathbf{D}^T and \mathbf{D}^P are the molecular, thermal and pressure diffusion coefficients, respectively.

Among these mechanisms, thermal diffusion plays a distinct role in mixtures exposed to temperature gradients. This phenomenon, known as the Soret effect, was first reported by Charles Soret in 1879, who observed that a salt solution under a temperature gradient developed a non-uniform concentration profile (SORET, 1879 apud DE GROOT and MAZUR, 1984).

The intensity of thermal diffusion is often characterized by the Soret coefficient:

$$S_{T,i} = \frac{D_i^T}{D_{ii}} \quad (2.46)$$

The Soret coefficient indicates the direction and strength of component flux induced by temperature gradients. Positive values are associated with components migrating toward colder regions, and negative values with movement toward warmer regions.

In practice, its direct measurement is often difficult. In most cases, the changes in concentration are small and convective flow can impact the result. Early experiments used vertical columns under a fixed temperature gradient and measured concentration at steady state, as in Soret experiments. More recent techniques include optical methods such as thermal diffusion forced Rayleigh scattering (TDFRS) and Rayleigh interferometry, and experiments in microgravity. A detailed review of these techniques is provided by RAHMAN and SAGUIR (2014).

Experimental data are mostly limited to binary and ternary mixtures, usually involving gases, simple liquids, or light hydrocarbons. Experimental data remain scarce for real reservoir fluid, high-pressure systems, or mixtures with heavy components such as asphaltenes (RAHMAN and SAGUIR, 2014).

The limited experimental data create difficulties for reservoir simulation. In practice, Soret coefficients for complex fluids are often estimated using theoretical models, molecular dynamics simulations, or calibrated through sensitivity analysis. Uncertainty in these values can affect long-term predictions of composition changes, especially in reservoirs with significant temperature gradients.

A complete derivation of the matrix form of the phenomenological laws and the associated flux–force structure is provided in Appendix B, following the formulation of DE GROOT and MAZUR (1984).

The next chapter presents the main models commonly used to describe multicomponent thermal diffusion in hydrocarbon systems and outlines how each framework represents the thermal contribution to mass transport.

Chapter 3

Literature Review on Multicomponent Thermal Diffusion

Several mathematical formulations have been proposed to describe molecular diffusion, gravitational segregation, and thermal diffusion in multicomponent mixtures (ESPÓSITO *et al.*, 2017). This chapter presents the models most relevant to the present study and summarizes the theoretical ideas on which they are based.

3.1 Firoozabadi's Model

Firoozabadi's model is derived within the framework of irreversible thermodynamics. It was originally proposed for binary mixtures (SHUKLA and FIROOZABADI, 1998) and later extended to nonideal multicomponent systems in the formulation of GHORAYEB and FIROOZABADI (2000a). The presentation in this section follows the derivation described by FIROOZABADI (2016), which provides a clear discussion of the main theoretical elements underlying the model.

Based on the general formulation described in Equation 2.45, Firoozabadi's model expresses the total flux as a combination of molecular, thermal, and pressure related contributions, each defined by a corresponding diffusion coefficient matrix.

The molecular diffusion coefficients D_{ij} are derived from the gradients of chemical potential with respect to composition at constant temperature and pressure. Non-ideal effects are included through the derivatives of fugacity. The expanded form, expressed in terms of molar masses M , mole fractions x , and fugacity derivatives, is:

$$D_{ij} = a_{in} D_{in} \frac{M_i x_i}{L_{ii}} \sum_{k=1}^{n-1} L_{ik}^{n-1} \sum_{l=1}^{n-1} \frac{M_l x_l + M_n x_n \delta_{lk}}{M_l} \frac{\partial \ln f_l}{\partial x_j} \Bigg|_{x_j, T, P} \quad (3.1)$$

The coefficients D_{in} and a_{in} are given by:

$$D_{in} = \frac{M^2 R L_{ii}}{c M_i^2 M_n^2 x_i x_n} \quad (3.2)$$

$$a_{in} = \frac{M_i M_n}{M^2} \quad (3.3)$$

The pressure diffusion coefficients D_i^P , as with the molecular coefficients, are derived from the gradients of chemical potential with respect to pressure, at constant temperature and composition. Expressed in terms of molar mass, mole fraction, and partial molar volumes \bar{V} , the formulation becomes:

$$D_i^P = a_{in} D_{in} \frac{M_i x_i}{R T L_{ii}} \sum_{k=1}^{n-1} L_{ik} \left[\sum_{j=1}^{n-1} x_j \bar{V}_j + \frac{M_n x_n}{M_k} \bar{V}_k - \frac{1}{c} \right] \quad (3.4)$$

The pressure and molecular diffusion expressions are coupled through the same phenomenological coefficients L_{ik} and L_{ii} , since both are derived from the difference in chemical potential gradients present in the expression for diffusion flux, as shown in Equation 2.44. Once the molecular diffusion coefficients are determined, the Onsager coefficients can be obtained and used directly in the pressure diffusion formulation.

To express thermal diffusion in the same structure used for molecular and pressure diffusion, the coefficient D_i^T is written in terms of the coefficients D_{in} and a_{in} , and the thermal diffusion ratio k_{T_i} .

$$D_i^T = a_{in} D_{in} M \frac{k_{T_i}}{T} \quad (3.5)$$

$$k_{T_i} = \frac{M_i x_i M_n x_n L_{iq}}{M R T L_{ii}} = \alpha_{T_i} x_i x_n \quad (3.6)$$

where α_{T_i} is the thermal diffusion factor.

This form simplifies the calculation of thermal diffusion using the same input applied to the other diffusion terms.

The phenomenological coefficient L_{iq} is related to the other Onsager coefficients through the net heat of transport Q_k^* . The net heat of transport represents the difference between the heat carried by the diffusive flux of component k and the average heat carried by the mixture. This quantity incorporates both equilibrium and non-equilibrium contributions and reflects how the component exchanges energy through molecular motion.

The relation between coefficients L_{iq} and L_{ik} is as follows:

$$L_{iq} = \sum_{k=1}^{n-1} L_{ik} \left(\frac{Q_k^*}{M_k} - \frac{Q_n^*}{M_n} \right) \quad (3.7)$$

The net heat of transport is calculated as:

$$Q_i^* = -\frac{\Delta\bar{U}_i}{\tau_i} + \left[\sum_{j=1}^n \frac{x_j \Delta\bar{U}_j}{\tau_j} \right] \frac{\bar{V}_i}{\sum_{j=1}^n x_j \bar{V}_j} \quad (3.8)$$

where $\Delta\bar{U}_i$ is the partial molar internal energy, \bar{V}_i is the partial molar volume, and τ_i is a parameter defined as:

$$\tau_i = \frac{\Delta U_i^{\text{vap}}}{\Delta U_i^{\text{vis}}} \quad (3.9)$$

where ΔU_i^{vap} is the energy of vaporization of pure component i and ΔU_i^{vis} is the energy of viscous flow of pure component i .

In the model, τ_i is treated as an adjustable parameter. Calculated values can range from 3 to 5 at low temperature and pressure, with 4 adopted as a good initial estimate (ESPÓSITO *et al.*, 2017; FIROOZABADI *et al.*, 2000).

The model enables the estimation of diffusion coefficients using thermodynamic properties derived from an equation of state and viscosity data. While it provides a consistent framework for including thermal and pressure effects, its predictive accuracy depends on the proper selection or calibration of the parameter τ_i and on the quality of the available fluid characterization data.

3.2 Espósito et al. correlation

In a systematic review of thermal diffusion models, ESPÓSITO *et al.* (2017) highlighted the strong influence of the parameter τ_i in Firoozabadi's formulation. Earlier applications often used a fixed value, usually $\tau_i = 4$ for hydrocarbons, but this approximation does not always reproduce compositional grading correctly. In some conditions, it produced unrealistic profiles or even predicted incorrect gas–oil contacts.

To improve the description of τ_i , ESPÓSITO *et al.* (2017) proposed an empirical correlation based on component molar mass and the reduced temperature of the mixture. The correlation is written as:

$$\tau_i = M_i^\beta e^\alpha \quad (3.10)$$

with the exponents defined as

$$\alpha = \alpha_0 + \alpha_1 T_r \quad (3.11)$$

$$\beta = \beta_0 + \frac{\beta_1}{T_r} \quad (3.12)$$

and $T_r = T/T_c$ is the reduced temperature of the mixture. The parameters α_0 , α_1 , β_0 and β_1 are adjusted to the dataset considered.

The correlation was applied to different cases, with specific parameter sets adjusted in each one. In Yufutsu field in Japan (GHORAYEB *et al.*, 2000), it reproduced the unusual inverted density profile and methane distribution better than both the isothermal model and the version with constant τ . The parameters were calibrated directly to the experimental data from this field.

In the high-temperature reservoir, representing a Brazilian offshore case, another set of coefficients was obtained:

$$\alpha_0 = -2.17078, \quad \alpha_1 = 4.07908, \quad \beta_0 = -2.71298, \quad \beta_1 = 3.39140 \quad (3.13)$$

This calibration worked well for Brazilian offshore reservoir conditions, where oils are usually found at high temperature and pressure. The correlation is not universal, but its form allows the parameters to be tuned for each fluid system. In the Brazilian case, the fitted values gave good results, which makes this version especially relevant for oil reservoirs in our context.

All the simulations in this work used the Brazilian calibration because it gives reliable results and matches the type of reservoirs studied here.

3.3 Pedersen's Model

The model of PEDERSEN and LINDELOFF (2003) adapts Haase's approach (HAASE, 1969) to describe the temperature effect. The fugacity equilibrium equation is modified by adding a term based on the specific enthalpy. The equation describing the variation of component i with depth z is:

$$RT \ln \left(\frac{\phi_i^z x_i^z P^z}{\phi_i^{z_{\text{ref}}} x_i^{z_{\text{ref}}} P^{z_{\text{ref}}}} \right) = M_i g(z - z_{\text{ref}}) - M_i \left(\frac{\bar{H}}{M} - \frac{\bar{H}_i}{M_i} \right) \frac{\Delta T}{T} \quad (3.14)$$

where z and z_{ref} are the depth and the reference depth, ϕ_i is the fugacity coefficient of component i , H is the molar enthalpy of the mixture, and \bar{H}_i is the partial molar enthalpy of component i .

The partial molar enthalpy is given by:

$$\bar{H}_i = H_i^{\text{ig}} + \bar{H}_i^{\text{res}} \quad (3.15)$$

where H_i^{ig} is the ideal-gas enthalpy and \bar{H}_i^{res} is the partial molar residual enthalpy.

The residual term can be calculated using a cubic EoS as:

$$\bar{H}_i^{\text{res}} = -RT^2 \frac{\partial \phi_i}{\partial T} \quad (3.16)$$

The ideal-gas enthalpy is treated as an adjustable parameter to match experimental data. In the absence of such data, it can be estimated from tabulated heat-capacity values. The model indicates that components with specific enthalpies higher than the mixture average tend to segregate toward warmer regions, while those with lower values migrate toward cooler regions.

3.4 Montel's Model

The formulation of BAGHOOEE *et al.* (2021); MONTEL *et al.* (2019) is based on irreversible thermodynamics and replaces empirical parameters with coefficients that can be connected to measurable fluid and reservoir properties, such as diffusion coefficients, viscosity, permeability, and thermodynamic derivatives. The molar flux of a component i is expressed as:

$$\mathbf{J}_i = -n_i L_P \left(\frac{V \nabla P - M \mathbf{g}}{T} \right) + n_i \frac{L_i}{T} (q_i \nabla T - \nabla_T \mu_i + M_i \mathbf{g}) \quad (3.17)$$

where n_i is the number of moles of component i , V the molar volume, M_i the molar mass of component i , M the mixture molar mass, \mathbf{g} the gravitational acceleration, T the temperature, μ_i the chemical potential of component i , q_i the partial molar heat of transport of component i , and L_P and L_i the phenomenological coefficients.

Although the term q_i is referred to as the heat of transport, it does not possess units of heat (J). Instead, it has units of entropy (J/K) and is defined as the residual entropy of component i .

$$q_i = s_i - s_i^* = s_i^{\text{res}} \quad (3.18)$$

This definition allows the model to capture the effect of entropy in thermal diffusion in a direct way.

The term L_i is the phenomenological coefficient associated with molecular diffusion process. Comparing to the matrix form of the terms L_{ij} , it corresponds to the diagonal term L_{ii} when considering the cross-effect terms $L_{ij} = 0$ for $i \neq j$.

$$L_i = \frac{D_i}{R \left(1 + x_i \frac{\partial \ln \phi_i}{\partial x_i} \right)} \quad (3.19)$$

where D_i is the molecular diffusion coefficient, and ϕ_i the fugacity coefficient.

The parameter L_D is defined as a combination of the L_i values:

$$\frac{1}{L_D} = \sum_i \frac{x_i}{L_i} \quad (3.20)$$

L_D is an auxiliary coefficient that balances the contributions of all L_i and provides the diffusion property of the mixture.

The last coefficient, L_P , appears in the term proportional to the pressure gradient and is written as

$$L_P = \frac{\rho}{M} \cdot \frac{Tk}{\eta} \quad (3.21)$$

where ρ the mixture density, k the permeability, and η the viscosity.

Together, these three coefficients structure the formulation. L_i introduces molecular diffusion corrected by non-ideal thermodynamics, L_D ensures the consistency of the multicomponent system, and L_P incorporates the role of pressure-driven transport through porous media. Their explicit dependence on measurable quantities is what allows the model to operate without arbitrary fitting parameters.

3.4.1 Derivations from Montel's Model

One of the objectives of this work is to test Montel's formulation for thermal diffusion in a reservoir simulation framework. To achieve this, the thermal diffusion coefficient derived from Montel's equations was implemented in the simulator. The existing structure of the code already accounts for molecular and pressure diffusion following Firoozabadi's model, and these contributions were not changed. Only the thermal diffusion term was introduced.

In Montel's original formulation, the coefficients L_i are obtained from molecular diffusion and thermodynamic derivatives. In this work, however, L_i is treated as an adjustable parameter, defined once for each pseudocomponent. This represents a methodological hypothesis designed to explore how Montel's thermal diffusion expression behaves when compared with other models. The formulation remains consistent with the original structure, but the adjustable L_i gives the flexibility required to test its performance against available data.

The thermal contribution in Equation 3.17 can be isolated, since the temperature gradient enters only through the $q_i \nabla T$ term. Rewriting this part in the transport formalism, the thermal flux of component i is expressed as

$$\mathbf{J}_i^T = n_i \frac{L_i}{T} q_i \nabla T \quad (3.22)$$

Using the relation $n_i = \rho x_i / M$, the flux becomes

$$\mathbf{J}_i^T = \frac{\rho}{M} x_i L_i \frac{q_i}{T} \nabla T \quad (3.23)$$

Comparing with the standard transport form, the thermal diffusion flux in molar basis is expressed as

$$\mathbf{J}_i^T = -D_i^T \nabla T \quad (3.24)$$

The thermal diffusion coefficient is

$$D_i^T = -\frac{\rho}{M} x_i L_i \frac{q_i}{T} \quad (3.25)$$

If the simulator is configured in mass basis rather than molar basis, the conversion can be carried out by using the molar density $c = \rho/M$ as a multiplicative factor, ensuring consistency between the two conventions. This procedure allows the formulation to be implemented in either framework without ambiguity.

Chapter 4

Methodology

This chapter presents the methodology used to evaluate thermal diffusion models in compositional reservoir simulations. The objective is to implement and compare different formulations for thermal diffusion coefficients, assess their impact on fluid distribution, and verify their consistency with experimental and field data.

Section 4.1 presents the simulator used and the numerical formulation applied. Section 4.2 describes the parameter regression performed for CO₂ and its impact on compositional fitting. Section 4.3 evaluates Montel's modified model and compares its performance with alternative formulations.

4.1 Compositional Reservoir Simulator

The reservoir simulator used in this study was originally developed as part of a research partnership between the ATOMS Laboratory (COPPE/UFRJ), the Reservoir Engineering Research Institute (RERI), and Petrobras. Written in Fortran, the code has been continuously expanded to support advanced compositional modeling, including the effects of molecular diffusion, thermal diffusion, and gravitational segregation in reservoir fluids.

In this study, the simulator is applied to one-dimensional steady-state problems, predicting vertical profiles of pressure, density, and composition from a specified reference condition. Thermodynamic properties, such as compressibility factor, fugacity, and enthalpy, are computed using the Peng–Robinson EoS.

The simulator uses two main input files. The first describes the fluid at the reference depth, including the list of components, their mole fractions, and thermodynamic properties such as critical pressure and temperature, molecular weight, acentric factor, binary interaction coefficients, and volume shift. These data are used to calculate phase behavior with the equation of state.

The second file contains information about reservoir data and control parameters. It includes the number of grid cells, reservoir dimensions, porosity, permeability,

initial pressure and temperature, and the temperature gradient. It also defines simulation options, such as whether the composition is given on a molar or mass basis, the molecular diffusion model to be used and the number of timesteps.

From the composition and thermodynamic properties specified at the reference depth, the simulator computes the pressure, density, and composition profiles along the vertical grid using the diffusion formulations described in section 3.1. The model includes the effects of molecular diffusion, thermal diffusion, and gravitational segregation. The thermal diffusion coefficient is calculated using the correlation proposed by ESPÓSITO *et al.* (2017), incorporated into the original formulation of GHORAYEB and FIROOZABADI (2000a).

In steady-state conditions, there is no net mass flow in the system, so the total molar diffusive flux of each component vanishes. This condition remains valid even in the presence of composition, pressure, and temperature gradients.

The simulator uses this principle to compute the variation of composition and pressure along the vertical column. Starting from a known reference state, the composition and pressure of the next grid block are found by solving a nonlinear system that satisfies the conditions of zero total diffusive flux and hydrostatic equilibrium.

The pressure in each new cell is calculated from the hydrostatic equation, which depends on the density of the fluid. Since density varies with composition, pressure is also treated as a variable that adjusts during the solution.

The nonlinear system consists of n equations and n unknowns, where the unknowns are the $n - 1$ mole fractions and the pressure. The equations that define the system are written as:

$$J_i(x_0, x, P_0, P, T_0, T) = 0, \quad i = 1, \dots, n - 1. \quad (4.1)$$

$$P - [P_0 - \rho g(z - z_0)] = 0, \quad \rho = \rho(x). \quad (4.2)$$

This system is solved iteratively using the Newton–Raphson (NR) method. Once the solution for a given cell converges, that cell becomes the new reference for computing the next one. This sequential procedure is known as homotopic continuation of zero order.

The vector of unknowns \mathbf{x} and the residual vector \mathbf{R} are:

$$\mathbf{x} = \{x_1, x_2, \dots, x_{n-1}, P\} \quad (4.3)$$

$$\mathbf{R}(\mathbf{x}) = \begin{bmatrix} f_1(x_1, x_2, \dots, x_{n-1}, P) \\ f_2(x_1, x_2, \dots, x_{n-1}, P) \\ \vdots \\ f_{n-1}(x_1, x_2, \dots, x_{n-1}, P) \\ f_n(x_1, x_2, \dots, x_{n-1}, P) \end{bmatrix} \quad (4.4)$$

Given an initial guess \mathbf{x}_0 , each iteration updates \mathbf{x} as:

$$\mathbf{x} = \mathbf{x}_0 - \mathbf{Jac}^{-1}(\mathbf{x}_0)\mathbf{R}(\mathbf{x}_0) \quad (4.5)$$

with the Jacobian defined by:

$$Jac_{ij} = \frac{\partial R_i}{\partial x_j} \quad (4.6)$$

Equation 4.1 is discretized as:

$$\begin{aligned} f_i &= \sum_{j=1}^{n-1} \left[\frac{D_{ij} + D_{0,ij}}{2} (x_j - x_{0,j}) \right] \\ &+ \frac{D_i^T + D_{0,i}^T}{2} (T - T_0) \\ &+ \frac{D_i^P + D_{0,i}^P}{2} (P - P_0), \quad i = 1, \dots, n-1. \end{aligned} \quad (4.7)$$

and Equation 4.2 as:

$$f_n = (P - P_0) + \frac{(\rho + \rho_0)}{2} g \Delta z \quad (4.8)$$

The analytical derivatives used to assemble the Jacobian are:

$$\frac{\partial f_i}{\partial x_j} = \frac{D_{ij} + D_{0,ij}}{2} \quad (4.9)$$

$$\frac{\partial f_i}{\partial P} = \frac{D_i^P + D_{0,i}^P}{2} \quad (4.10)$$

$$\frac{\partial f_n}{\partial x_j} = 0 \quad (4.11)$$

$$\frac{\partial f_n}{\partial P} = 1 \quad (4.12)$$

$$\mathbf{Jac} = \begin{bmatrix} \frac{D_{1,1} + D_{0,1,1}}{2} & \frac{D_{1,2} + D_{0,1,2}}{2} & \dots & \frac{D_{1,n-1} + D_{0,1,n-1}}{2} & \frac{D_1^P + D_{0,1}^P}{2} \\ \frac{D_{2,1} + D_{0,2,1}}{2} & \frac{D_{2,2} + D_{0,2,2}}{2} & \dots & \frac{D_{2,n-1} + D_{0,2,n-1}}{2} & \frac{D_2^P + D_{0,2}^P}{2} \\ \vdots & \vdots & \ddots & \vdots & \vdots \\ \frac{D_{n-1,1} + D_{0,n-1,1}}{2} & \frac{D_{n-1,2} + D_{0,n-1,2}}{2} & \dots & \frac{D_{n-1,n-1} + D_{0,n-1,n-1}}{2} & \frac{D_{n-1}^P + D_{0,n-1}^P}{2} \\ 0 & 0 & \dots & 0 & 1 \end{bmatrix} \quad (4.13)$$

4.2 Parameter regression of τ_{CO_2} for depth-dependent compositional grading

The study focuses on a reservoir located in the Santos Basin, primarily characterized by a natural gas accumulation with a gas cap containing a very high CO_2 content (70–80%). This reservoir was selected because its CO_2 -rich gas cap exhibits a pronounced compositional gradient that could not be matched using the assumptions of constant τ_i in the models of Firoozabadi or Espósito, motivating the investigation of an alternative formulation.

In Firoozabadi’s formulation, the thermal diffusion coefficient is expressed in terms of a fitting parameter τ_i , typically assumed to be constant throughout the system. This parameter is defined as the ratio between the energy of vaporization and the energy of viscous flow of the pure component. The model generally adopts $\tau_i = 4$ for all components, and does not specify a particular value for CO_2 . In all cases, the value is assumed constant across the reservoir, regardless of depth or composition (FIROOZABADI *et al.*, 2000).

ESPÓSITO *et al.* (2017) proposed a correlation for τ_i that introduces dependency on composition and temperature, allowing the parameter to vary across the reservoir. The correlation was applied only to hydrocarbon components, while the CO_2 parameter remained unchanged, following the original fixed value approach. Reported values for τ_{CO_2} in their study ranged from 0.1 to 2.0.

In this study, the analysis is carried out by modifying Espósito’s (2017) formulation, extending the original correlation to include a depth-dependent expression for τ_{CO_2} . The objective is to examine whether this extension of Espósito’s model improves the match with measured compositional profiles.

4.2.1 Simulation Setup

To evaluate the effect of a depth-dependent τ_{CO_2} , the modified Esposito formulation was implemented in the simulator, applying the correlation originally proposed by ESPÓSITO *et al.* (2017) for hydrocarbon components to CO_2 as well. The formulation expresses τ_i as a function of molar mass and pseudoreduced temperature:

$$\tau_i = M_i^\beta e^\alpha \quad \alpha = \alpha_0 + \alpha_1 T_r \quad \beta = \beta_0 + \frac{\beta_1}{T_r}$$

where M_i is the molar mass of component i , and T_r is the pseudoreduced temperature.

The four correlation coefficients ($\alpha_0, \alpha_1, \beta_0, \beta_1$) were treated as fitting parameters and provided as input to the simulator.

A Python script, developed by the author specifically for this study, was used to manage the optimization loop. For each trial, it proposed a new set of coefficients, ran the simulator with the current inputs, retrieved the composition profile, and evaluated the objective function based on the difference between the simulated and experimental compositions. This process was repeated until the optimizer converged to a minimum.

The best result obtained with the optimized correlation was then compared with simulations using predefined constant values of τ_{CO_2} , within the range suggested by ESPÓSITO *et al.* (2017) (0.1, 0.5, 1.0, and 2.0).

After identifying the best-fit correlation, a second test was carried out to evaluate whether it could also help estimate a suitable fixed value for τ_{CO_2} . The goal was to provide a practical alternative for cases in which the simulator cannot be modified to support a depth-dependent formulation. In such scenarios, having a predictive expression for τ_{CO_2} may help avoid trial-and-error calibration. For this test, the optimized correlation was evaluated at the reference depth, and the resulting value was applied uniformly throughout the reservoir.

The Figure 4.1 illustrates the workflow used to calibrate the thermal-diffusion parameter. A vector of trial parameters $\boldsymbol{\kappa}$ is proposed by the optimizer and passed to the compositional reservoir simulator. The simulator computes the resulting vertical composition profile $x_i(z, \boldsymbol{\kappa})$, which is then compared against the measured experimental profile x_{exp} . This comparison is performed through an objective function, which quantifies the mismatch between simulated and measured data. The resulting objective-function value f_{obj} is returned to the optimizer, which updates $\boldsymbol{\kappa}$ and repeats the loop until convergence. This representation highlights the flow of information between the optimizer, the simulator, and the experimental data, making the calibration sequence explicit.

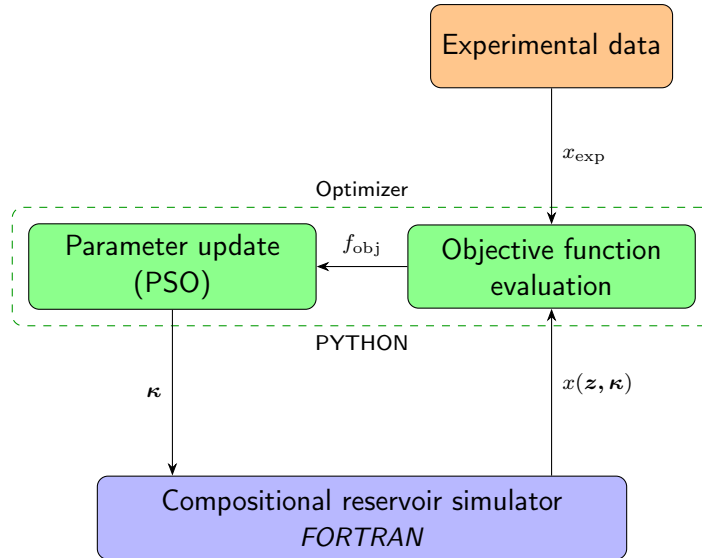


Figure 4.1: Optimization loop integrating experimental data, the Python-based optimizer, and the compositional reservoir simulator.

4.2.2 Fluid Description

For this study, six PVT analyses from a single producing well were available, each corresponding to a different sampling depth. One sample, corresponding to a relative depth of 108 m, was used as the reference composition for the simulator. This depth was selected arbitrarily as a convenient datum for plotting and simulation purposes. At this reference depth, the reservoir conditions are $T = 338.75$ K and $P = 621.32$ bar, with a vertical temperature gradient of 0.024 K/m.

For the reference-depth PVT sample, the heavy-end fraction was first split into two fractions using the Shibata methodology (see subsection 2.4.1). The complete composition was then processed using a compositional fluid characterization tool, where component lumping was performed and the fluid was tuned to the Peng–Robinson EoS (see section 2.5). The resulting fluid property tables, which were used as input to the simulator, are presented in Table 4.1 and Table 4.2.

The remaining five PVT samples were expressed in the same pseudocomponent structure by summing the mole fractions accordingly, as shown in Table 4.3. These compositions were used as experimental inputs in the objective function to evaluate the deviation between simulation results and measured data.

4.2.3 Optimization Strategy

The objective function minimizes the sum of squared differences between simulated and experimental fluid compositions. This approach is commonly used because it is straightforward to compute and effectively captures deviations between model and data:

Table 4.1: Mole fractions and thermodynamic properties of pseudocomponents at the reference depth (108 m).

PComp.	Mole Fraction	M (g/mol)	T _c (K)	P _c (bar)	ω
CO ₂	0.5601	44.01	304.2	72.8	0.2250
N ₂ -C ₁	0.1624	16.23	189.6	44.64	0.0082
C ₂ -C ₅	0.0379	43.47	366.2	42.12	0.1400
C ₆ -C ₁₂	0.0322	145.73	546.2	25.27	0.5300
C ₁₃ -C ₁₉	0.0342	241.47	678.1	16.2	0.8100
Resin	0.1602	540	984.2	10.5	1.1800
Asphaltene	0.0130	1500	1212.5	5.48	1.7200

Table 4.2: Binary interaction coefficients for the adjusted fluid at the reference depth (108 m).

	CO ₂	N ₂ -C ₁	C ₂ -C ₅	C ₆ -C ₁₂	C ₁₃ -C ₁₉	Resin	Asphaltene
CO ₂	0.0000	0.1500	0.1400	0.1200	0.1000	0.1047	0.0729
N ₂ -C ₁	0.1500	0.0000	0.0269	0.0300	0.0440	0.0772	0.1847
C ₂ -C ₅	0.1400	0.0269	0.0000	0.0000	0.0000	0.0000	0.0000
C ₆ -C ₁₂	0.1200	0.0300	0.0000	0.0000	0.0000	0.0000	0.0000
C ₁₃ -C ₁₉	0.1000	0.0440	0.0000	0.0000	0.0000	0.0000	0.0000
Resin	0.1047	0.0772	0.0000	0.0000	0.0000	0.0000	0.0000
Asphaltene	0.0729	0.1847	0.0000	0.0000	0.0000	0.0000	0.0000

$$S(\boldsymbol{\kappa}) = \sum_z \sum_i (x_{\text{exp},i}(z) - x_i(z, \boldsymbol{\kappa}))^2 \quad (4.14)$$

The C₂₀₊ fraction was not included in the objective function, as it is distributed between heavy pseudocomponents in the model and would require additional post-processing to isolate consistently across depths.

To ensure realistic results, a penalty term r was added to the objective function. Values of τ_{CO_2} below zero are not physically valid, while values above 10 are considered excessively high based on values reported in the literature. The constraint is enforced by penalizing any coefficient set that leads to values outside the acceptable range at any depth:

$$P(\boldsymbol{\kappa}) = S(\boldsymbol{\kappa}) + r [\max(0, -\tau_{\text{CO}_2}) + \max(0, \tau_{\text{CO}_2} - 10)] \quad (4.15)$$

If the simulator fails to converge for a given trial, the penalty is increased to ten times the restriction value ($10r$). The optimization stops when the absolute difference between successive $P(\boldsymbol{\kappa})$ values falls below 10^{-6} .

A Particle Swarm Optimization (PSO) scheme was used to estimate the four correlation coefficients $\boldsymbol{\kappa} = (\alpha_0, \alpha_1, \beta_0, \beta_1)$ defining τ_{CO_2} . PSO searches for the

Table 4.3: Pseudocomponent compositions for the remaining five PVT samples at different depths.

PComp.	96 m	136.3 m	146.5 m	152.8 m	208 m
CO ₂	0.5435	0.6001	0.6070	0.7714	0.7719
N ₂ -C ₁	0.1654	0.1604	0.1550	0.1683	0.1724
C ₂ -C ₅	0.0371	0.0347	0.0323	0.0269	0.0250
C ₆ -C ₁₂	0.0446	0.0381	0.0402	0.0156	0.0128
C ₁₃ -C ₁₉	0.0528	0.0416	0.0522	0.0113	0.0088
C ₂₀₊	0.1566	0.1732	0.1133	0.0065	0.0091

global minimum through function evaluations, without requiring gradients, starting from a stochastic swarm of particles randomly initialized across the search domain. This makes it suitable for irregular, nonlinear, and discontinuous search spaces.

After the PSO runs, the best solution was refined using Powell’s method for local optimization.

The swarm is initialized with N_p particles, each holding a candidate vector $\boldsymbol{\kappa}_j^0$. At each iteration, the velocity of particle j is updated as:

$$\mathbf{v}_j^{k+1} = w \mathbf{v}_j^k + c_1 r_1 (\mathbf{pBest}_j - \boldsymbol{\kappa}_j^k) + c_2 r_2 (\mathbf{gBest} - \boldsymbol{\kappa}_j^k) \quad (4.16)$$

$$\boldsymbol{\kappa}_j^{k+1} = \boldsymbol{\kappa}_j^k + \mathbf{v}_j^{k+1} \quad (4.17)$$

where $\boldsymbol{\kappa}_j^{k,k}$ is the position of particle j at iteration k , $\mathbf{v}_j^{k,k}$ is its velocity, \mathbf{pBest}_j is its best-known position, \mathbf{gBest} is the global best-known position, w is the inertia weight, c_1 and c_2 are the cognitive and social parameters, and r_1 and r_2 are random numbers between 0 and 1.

Powell’s method starts with n orthogonal search directions, n being the number of components in $\boldsymbol{\kappa}$. It performs one-dimensional line searches along each direction, updating the point after each step. After all directions are swept, the overall displacement vector replaces the one producing the largest objective reduction, forming a new set of n directions for the next iteration.

Sensitivity runs assessed the effect of the penalty factor r (0.1, 1, 10), swarm size (100 and 200 particles), and tolerance (10^{-4} , 10^{-6}). The selected PSO configuration is given in Table 4.4.

A total of 25 data points were used to compute the objective function, combining five pseudocomponents across five different depths. These were compared against the simulation results at matching depths to guide the optimization. The regression involves four fitting parameters. Results, including a comparison with fixed-value

Table 4.4: Configuration of the Particle Swarm Optimization algorithm used for parameter regression.

Parameter	Value
Number of independent minimization	10
Penalty factor (r)	1
Search range for each variable	$[-10, 10]$
Swarm population	100
Generations	100
Objective tolerance	10^{-6}
Inertia weight (w)	0.5
Cognitive coefficient (c_1)	0.5
Social coefficient (c_2)	0.5

scenarios, are presented in Section 5.1.

4.3 Parameter Regression for the Montel’s Modified Thermal Diffusion Model

In this part of the study, Montel’s thermal diffusion formulation (BAGHOOEE *et al.*, 2021; MONTEL *et al.*, 2019) is used as the starting point. The model was adapted so that the Onsager coefficient L_i becomes an adjustable parameter for each pseudocomponent, leading to what is referred to here as Montel’s modified model. This version was implemented in the simulator and calibrated against measured compositional profiles to explore how well it can reproduce multicomponent grading under non-isothermal conditions (see subsection 3.4.1).

Since the work focuses on extending and calibrating Montel’s formulation, the modified model is the main approach examined in this section. The original models of FIROOZABADI *et al.* (2000), ESPÓBITO *et al.* (2017), and PEDERSEN and LINDELOFF (2003) are included as reference cases. Their results offer a useful baseline for comparing the modified formulation and assessing the impact of allowing component-specific adjustable coefficients.

4.3.1 Simulation setup

To implement Montel’s thermal diffusion formulation in the simulator, its expression for the thermal diffusion coefficient was analyzed for consistency with the existing numerical framework.

From this analysis, the thermal diffusion coefficient is expressed as:

$$\mathbf{D}_{\text{Montel}}^{\mathbf{T}} = x_i L_i \frac{q_i}{T} \quad (4.18)$$

where q_i is the heat of transport term, defined by Montel as $q_i = s_i^{\text{res}}$.

The simulator was modified to calculate Montel’s thermal diffusion coefficient. The residual entropy s_i^{res} was calculated as follows:

$$s_i^{\text{res}} = -R \ln \phi_i - RT \frac{\partial \ln \phi_i}{\partial T} - R \ln Z \quad (4.19)$$

In Montel’s original formulation, L_i was correlated with other diffusive parameters. In the modified version adopted here, L_i is instead treated as an adjustable parameter, assumed constant with depth for each pseudocomponent. This represents a deliberate methodological hypothesis, intended to explore how the model behaves under a simplified representation. By adopting this approach, the formulation could be tested at reservoir scale while keeping the role of the thermal diffusion term explicit and avoiding additional layers of dependence. The simulator was therefore modified to accept L_i as input, with values estimated through the optimization routine.

The optimization procedure follows the same general structure described in Section 4.2. An external Python routine generates trial values of L_i , runs the Fortran simulator, reads the output compositions, evaluates the objective function, and updates the parameters until convergence.

4.3.2 Fluid description

This study analyzes three reservoir fluids, selected to evaluate the modified Montel formulation. Referred to as Fields A, B and C, these datasets were chosen to progressively increase the level of complexity in the tests. Each field represents a distinct geological setting and exhibits its own degree of compositional variability.

Field A. Field A is based on a North Sea reservoir fluid originally used in MONTTEL *et al.* (2019) and BAGHOOEE *et al.* (2021). In those studies, compositional gradients were not obtained from field measurements but generated through Non-Equilibrium Molecular Dynamics (NEMD) simulations under both isothermal and non-isothermal conditions, with the corresponding plots presented in the original publications.

In this work, the same reference was adopted, with depth of -5525 m, temperature of 87.5 ° C, pressure of 641 bar, and geothermal gradient of 0.029 K/m. The NEMD generated points were considered as target data in the objective function. Since their numerical values were not reported explicitly in the original articles, they were extracted by digitizing the published figures. A total of ten depths were digitized,

one taken as the reference point and the remaining nine used in the comparison. For each depth, four components were considered, providing the set of experimental values used in the regression procedure.

The composition and thermodynamic properties used to describe the oil for Field A (molar mass, critical temperature, critical pressure, acentric factor, and volume shift) are presented in Table 4.5. Binary interaction parameters are presented in Table 4.6.

Table 4.5: Thermodynamic properties of pseudocomponents used to describe the oil of Field A.

Component	Mole fraction	M (g/mol)	T_c (K)	P_c (bar)	ω	C_i
N ₂ -C ₁	0.36273	16.12	190.26	46.33	0.0117	-0.220
CO ₂	0.37262	44.01	304.10	73.70	0.2389	-0.030
C ₂	0.04795	30.07	305.43	48.84	0.0986	-0.070
C ₃ -C ₄	0.05373	49.52	388.85	40.40	0.1653	-0.010
C ₅ -C ₁₀	0.06061	99.29	572.15	30.20	0.2924	0.020
C ₁₁ -C ₁₉	0.04948	196.19	728.15	20.60	0.4746	0.025
CN1	0.02849	331.82	883.15	15.20	0.7300	0.030
CN2	0.02439	569.31	1173.15	13.50	0.9790	0.035

Table 4.6: Matrix of binary interaction parameters (k_{ij}) for Field A.

	N ₂ -C ₁	CO ₂	C ₂	C ₃ -C ₄	C ₅ -C ₁₀	C ₁₁ -C ₁₉	CN1	CN2
N ₂ -C ₁	0.00	0.10	0.00	0.00	0.03	0.05	0.06	0.07
CO ₂	0.10	0.00	0.13	0.13	0.12	0.07	0.06	0.06
C ₂	0.00	0.13	0.00	0.00	0.01	0.02	0.02	0.02
C ₃ -C ₄	0.00	0.13	0.00	0.00	0.00	0.00	0.00	0.00
C ₅ -C ₁₀	0.03	0.12	0.01	0.00	0.00	0.00	0.00	0.00
C ₁₁ -C ₁₉	0.05	0.07	0.02	0.00	0.00	0.00	0.00	0.00
CN1	0.06	0.06	0.02	0.00	0.00	0.00	0.00	0.00
CN2	0.07	0.06	0.02	0.00	0.00	0.00	0.00	0.00

The estimated components for isothermal and non-isothermal cases are presented in Table 4.7, Table 4.8, Table 4.9, and Table 4.10.

Table 4.7: Depth and mole fraction of component N_2-C_1 for isothermal and non-isothermal cases of Field A.

Isothermal		Non-isothermal	
Depth (m)	Mole fraction	Depth (m)	Mole fraction
-5775.7	0.33677	-5776.7	0.36294
-5726.1	0.34180	-5726.1	0.36277
-5675.5	0.34801	-5676.5	0.36260
-5626.9	0.35388	-5625.9	0.36260
-5576.3	0.35958	-5575.3	0.36294
-5525.7	0.36528	-5526.7	0.36260
-5476.1	0.37031	-5475.1	0.36277
-5425.5	0.37484	-5426.5	0.36310
-5375.9	0.37870	-5374.9	0.36310
-5325.3	0.38273	-5325.3	0.36277

Table 4.8: Depth and mole fraction of component CO_2 for isothermal and non-isothermal cases of Field A.

Isothermal		Non-isothermal	
Depth (m)	Mole fraction	Depth (m)	Mole fraction
-5776.7	0.36536	-5777.7	0.37236
-5726.0	0.36751	-5727.0	0.37265
-5675.3	0.36938	-5675.3	0.37248
-5625.6	0.37121	-5625.6	0.37239
-5575.9	0.37245	-5575.9	0.37248
-5527.2	0.37392	-5526.2	0.37259
-5476.5	0.37561	-5475.5	0.37248
-5425.8	0.37632	-5425.8	0.37242
-5376.1	0.37673	-5374.0	0.37259
-5326.4	0.37670	-5325.4	0.37277

Table 4.9: Depth and mole fraction of component CN1 for isothermal and non-isothermal cases of Field A.

Isothermal		Non-isothermal	
Depth (m)	Mole fraction	Depth (m)	Mole fraction
-5775.1	0.03875	-5775.1	0.02859
-5725.2	0.03712	-5723.7	0.02859
-5674.6	0.03513	-5673.8	0.02865
-5624.8	0.03276	-5624.8	0.02865
-5574.9	0.03029	-5573.4	0.02856
-5525.1	0.02789	-5525.1	0.02849
-5475.2	0.02561	-5474.5	0.02837
-5425.4	0.02349	-5424.6	0.02833
-5375.5	0.02186	-5374.8	0.02833
-5324.9	0.02064	-5325.7	0.02833

Table 4.10: Depth and mole fraction of component CN2 for isothermal and non-isothermal cases of Field A.

Isothermal		Non-isothermal	
Depth (m)	Mole fraction	Depth (m)	Mole fraction
-5774.8	0.05002	-5774.8	0.02481
-5723.5	0.04275	-5723.5	0.02491
-5673.0	0.03538	-5673.8	0.02472
-5624.9	0.02889	-5625.7	0.02462
-5573.7	0.02336	-5573.7	0.02462
-5524.0	0.01861	-5523.2	0.02452
-5474.3	0.01512	-5474.3	0.02443
-5424.6	0.01221	-5423.8	0.02423
-5373.3	0.01028	-5373.3	0.02423
-5323.7	0.00863	-5323.7	0.02433

Field B. Field B corresponds to a carbonate reservoir in the Campos Basin, with reservoir depths between 5000 and 6000 m and a geothermal gradient of approximately 0.024 K/m. The fluid sampled in this field is a medium to heavy oil, with API gravity values between 17 ° and 22 °.

For this case, the available PVT data come from a single producing well. The reference composition used in the simulator corresponds to an oil sample collected at a relative depth of 93 m, associated with a pressure of 466.21 bar and a temperature

of 395.55 K. The target point used in the regression procedure is a gas sample taken at 351 m, which provides the compositional values included in the objective function. Only the mole fractions of the pseudocomponents reported at this target depth are used in the comparison, resulting in six objective-function terms. The reference sample serves solely as the initial composition for the simulation and is not part of the objective function.

Field B therefore introduces a real reservoir setting with limited vertical sampling and a transition that crosses the gas–oil contact. This change in fluid phase behavior makes the case more demanding for the modified Montel formulation than Field A, since the model must reproduce a compositional shift that reflects both equilibrium partitioning and the local thermal and gravitational conditions.

The compositions, thermodynamic properties, and binary interaction coefficients for Field B are given in Table 4.11, Table 4.12 and Table 4.13 respectively.

Table 4.11: Mole fraction of the pseudocomponents for Field B.

Pseudocomponent	93 m	351 m
CO ₂	0.0257	0.0295
N ₂ -C ₁	0.5685	0.7477
C ₂ -C ₅	0.1626	0.1411
C ₆ -C ₁₂	0.0992	0.0510
C ₁₃ -C ₁₉	0.0595	0.0207
C ₂₀₊		0.0097
QC24	0.0458	
QC43	0.0270	
QC70	0.0115	

Table 4.12: Thermodynamic properties of pseudocomponents for Field B

Pseudocomponent	T_C (K)	P_C (bar)	ω	M (g/mol)
CO ₂	304.20	73.76	0.2250	44.01
N ₂ -C ₁	189.99	45.90	0.0083	16.15
C ₂ -C ₅	376.00	41.70	0.2462	41.78
C ₆ -C ₁₂	606.73	30.67	0.2359	148.72
C ₁₃ -C ₁₉	732.45	21.76	0.4984	238.60
QC24	815.89	11.42	0.7906	364.30
QC43	959.82	7.71	1.2217	632.96
QC70	1343.33	7.01	1.2427	866.53

Field C. Field C corresponds to a carbonate reservoir located in the Santos Basin, at depths between 5500 and 6500 m, with a geothermal gradient of 0.02825 K/m.

Table 4.13: Values of binary interaction coefficients for Field B

	CO ₂	N ₂ -C ₁	C ₂ -C ₅	C ₆ -C ₁₂	C ₁₃ -C ₁₉	QC24	QC43	QC70
CO ₂	0.0000	0.2148	0.2048	0.1948	0.1848	0.1348	0.0948	0.2148
N ₂ -C ₁	0.2148	0.0000	0.0327	0.0415	0.0505	0.0631	0.0900	0.1027
C ₂ -C ₅	0.2048	0.0327	0.0000	0.2000	0.1987	0.0000	0.0000	0.0000
C ₆ -C ₁₂	0.1948	0.0415	0.2000	0.0000	0.0000	0.0000	0.0000	0.0000
C ₁₃ -C ₁₉	0.1848	0.0505	0.1987	0.0000	0.0000	0.0000	0.0000	0.0000
QC24	0.1348	0.0631	0.0000	0.0000	0.0000	0.0000	0.0000	0.0000
QC43	0.0948	0.0900	0.0000	0.0000	0.0000	0.0000	0.0000	0.0000
QC70	0.2148	0.1027	0.0000	0.0000	0.0000	0.0000	0.0000	0.0000

The reservoir contains a medium oil, with API gravity values between 28 ° and 31 °, and exhibits stronger compositional variation compared with the previous cases.

For this field, compositional data were obtained from three wells. Well 1 provided two production-test samples free from drilling-fluid contamination, and one of these samples was selected as the reference for the simulation. The reported depths correspond to the midpoints of the perforated intervals. The reference sample is associated with a relative depth of 210 m, at 915 bar and 369.15 K, and is used only as the initial condition for the model.

The second sample from Well 1, collected at 407 m, was included in the objective function. Seven pseudocomponents were reported for this depth, resulting in seven comparison points. Wells 2 and 3 contributed an additional set of twelve bottom-hole samples, with two measurements at each depth. For these samples, only two compositions were reported per depth, adding twenty-four points to the objective function. Altogether, Field C provides thirty-one compositional values for the regression procedure.

Field C is therefore the most challenging dataset in this study, combining multiple wells, mixed compositional resolution and stronger vertical gradients, and thus offering a broader basis for evaluating the performance of the modified Montel formulation.

The compositions of Well 1, thermodynamic properties, and binary interaction coefficients for Field C are listed in Table 4.14, Table 4.15 and Table 4.16 respectively. Compositions available for Wells 2 and 3 are presented in Table 4.17.

4.3.3 Optimization strategy

The optimization estimates the set of L_i values, assumed constant with depth, that minimizes the deviation between simulated and experimental mole fractions at the target points.

The objective function was defined as the sum of squared errors between simulated and experimental mole fractions at the target depths. For the C₂₀₊ fraction,

Table 4.14: Mole fraction of the pseudocomponents for Well 1 in Field C.

Pseudocomponent	210 m	407 m
CO ₂	0.0007	0.0012
N ₂ -C ₁	0.6416	0.6480
C ₂	0.0809	0.0816
C ₃ -C ₄	0.0782	0.0743
C ₅ -C ₁₂	0.0942	0.0981
C ₁₃ -C ₁₉	0.0445	0.0441
C ₂₀₊		0.0474
QC26	0.0487	
QC57	0.0112	

Table 4.15: Thermodynamic properties of pseudocomponents for Field C.

Pseudocomponent	T_C (K)	P_C (bar)	ω	M (g/mol)
CO ₂	304.20	72.80	0.2250	44.01
N ₂ -C ₁	189.99	45.30	0.0083	16.15
C ₂	305.40	48.20	0.0980	30.07
C ₃ -C ₄	389.02	40.03	0.1650	49.24
C ₅ -C ₁₂	573.52	29.42	0.2671	117.90
C ₁₃ -C ₁₉	726.86	18.99	0.5307	220.65
QC26	864.63	12.12	0.8623	378.18
QC57	1059.48	7.44	1.2926	804.73

the error was calculated as the difference between the sum of the split Shibata fractions from the reference sample and the reported C₂₀₊ fraction. Two penalty terms were also incorporated into the objective function, one proportional to the magnitude of any local increase in density toward the top of the column, and a fixed value of 100 applied whenever the simulator failed to identify a gas–oil contact (defined as a density decrease of at least 20 kg/m³ between consecutive depths). This ensured that the optimization favored both accurate compositional matching and physically consistent density trends.

Three methods were tested: Particle Swarm Optimization (PSO), Nelder–Mead and Powell. PSO yielded the lowest objective function values with reduced simulation time, and was therefore selected for the subsequent cases. The PSO implementation follows the formulation already presented in subsection 4.2.1 and uses the same parameter definitions.

Table 4.16: Values of binary interaction coefficients for Field C

	CO ₂	N ₂ -C ₁	C ₂	C ₃ -C ₄	C ₅ -C ₁₂	C ₁₃ -C ₁₉	QC26	QC57
CO ₂	0.0000	0.1500	0.1455	0.1416	0.1294	0.1089	0.0774	0.0000
N ₂ -C ₁	0.1500	0.0000	0.0079	0.0098	0.0159	0.0262	0.0420	0.1805
C ₂	0.1455	0.0079	0.0000	0.0000	0.0000	0.0000	0.0000	0.0000
C ₃ -C ₄	0.1416	0.0098	0.0000	0.0000	0.0000	0.0000	0.0000	0.0000
C ₅ -C ₁₂	0.1294	0.0159	0.0000	0.0000	0.0000	0.0000	0.0000	0.0000
C ₁₃ -C ₁₉	0.1089	0.0262	0.0000	0.0000	0.0000	0.0000	0.0000	0.0000
QC26	0.0774	0.0420	0.0000	0.0000	0.0000	0.0000	0.0000	0.0000
QC57	0.0000	0.1805	0.0000	0.0000	0.0000	0.0000	0.0000	0.0000

Table 4.17: Composition of the pseudocomponents for Wells 2 and 3 in Field C.

Sample	Depth (m)	N ₂ -C ₁	C ₂₀₊
Well 3	566	0.6600	0.0471
Well 3	566	0.6529	0.0473
Well 3	561	0.6496	0.0485
Well 3	561	0.6565	0.0476
Well 2	403	0.6548	0.0591
Well 2	403	0.6524	0.0581
Well 2	327	0.6523	0.0597
Well 2	327	0.6504	0.0603
Well 2	255	0.6532	0.0584
Well 2	255	0.6505	0.0600
Well 2	36	0.6496	0.0611
Well 2	36	0.6496	0.0583

Chapter 5

Results and Discussion

5.1 Results of Parameter Regression for τ_{CO_2}

In this experiment, the results correspond to the reservoir used in the modified Espósito formulation, which is a predominantly gas accumulation in the Santos Basin containing 70–80% CO_2 in the gas cap. This case was selected because previous studies showed that fixed values of τ_{CO_2} did not reproduce the observed CO_2 enrichment near the top of the reservoir, motivating the evaluation of a different approach for τ_{CO_2} .

To evaluate the impact of τ_{CO_2} on compositional grading, the implemented correlation with four adjustable parameters was compared with simulations in which τ_{CO_2} was assigned a fixed value. Simulations were first run with τ_{CO_2} values of 0.1, 0.5, 1.0, and 2.0, to cover the range proposed in the methodology. The results are presented, along with the experimental data, in Figure 5.1. For values of 0.5 or higher, the simulations are unable to capture the gas-oil contact, indicating that large τ_{CO_2} cannot reproduce the observed compositional gradient.

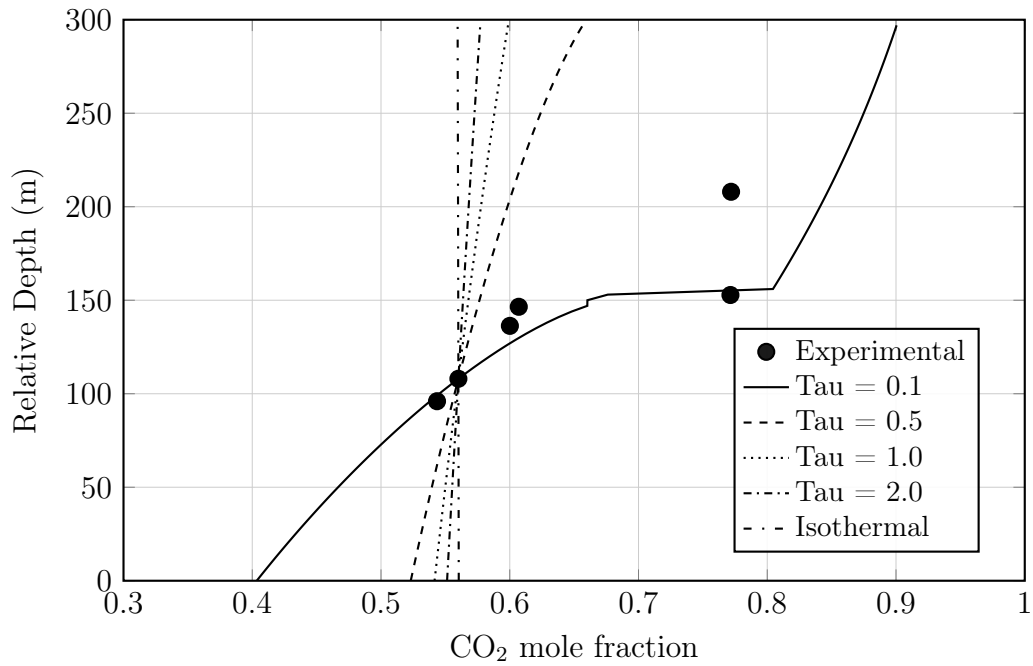


Figure 5.1: Simulated CO_2 profiles for fixed τ_{CO_2} values in the range of 0.1 to 2.0.

To explore the region where better matches seemed to occur, a second set of runs used smaller values (0.1, 0.15, 0.2, and 0.4). These values were not obtained from optimization, but chosen based on visual inspection of the first results. Figure 5.2 shows the profiles.

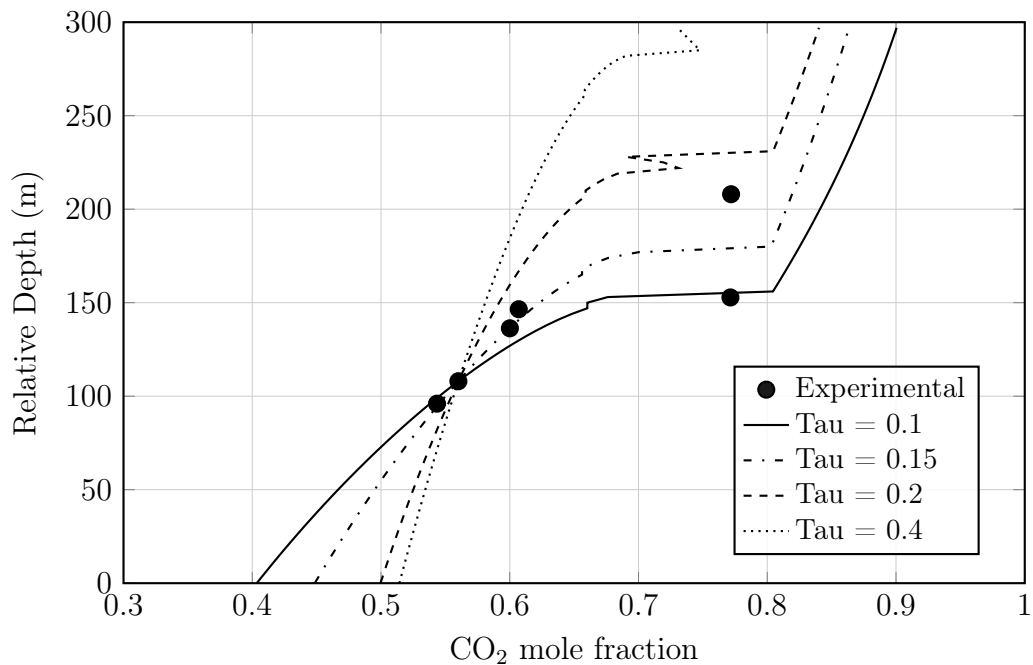


Figure 5.2: Simulated CO_2 profiles for fixed τ_{CO_2} values in the reduced range closer to the optimized value.

A comparison was made between the PSO-optimized τ_{CO_2} correlation and two

fixed value cases that visually provide the better results (0.1 and 0.15). As shown in Figure 5.3, the correlation resulted in a different profile, with a visible change in shape across the interval, particularly near the gas-oil transition.

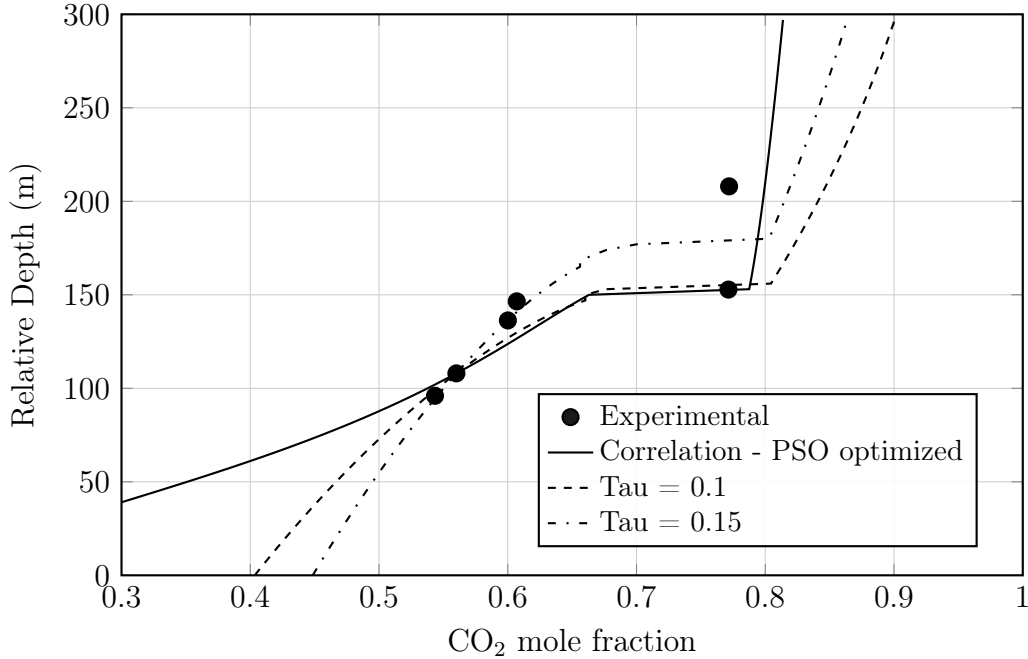


Figure 5.3: Comparison between correlation-based τ_{CO_2} (PSO optimized) and selected fixed-value simulations.

The corresponding τ_{CO_2} values from the correlation at each experimental depth are listed in Table 5.1. These values vary with depth, as the correlation depends on local thermodynamic conditions. In the oil zone, the values are around 0.6–0.7, and in the gas zone, they drop to approximately 0.05.

Table 5.1: τ_{CO_2} values from the PSO-optimized correlation at experimental depths

Relative Depth (m)	τ_{CO_2}
208	0.0560
152.8	0.1262
145.5	0.1591
136.3	0.6105
108	0.6696
96	0.6946

After the PSO run, Powell’s method was used as a local refinement. The change in the objective function was small (on the order of 10^{-5}), and some numerical instabilities appeared near the gas-oil transition. This same behavior was seen with the fixed value of 0.2 and 0.4, suggesting that the issue is related to the simulator’s sensitivity in that region, not to the optimization method.

Given these results, the PSO solution was retained as the final outcome, while the Powell step was applied only as a sensitivity check. Figure 5.4 compares the CO₂ mole fraction profiles obtained with and without Powell refinement. The corresponding objective function values and parameter sets are listed in Table 5.2.

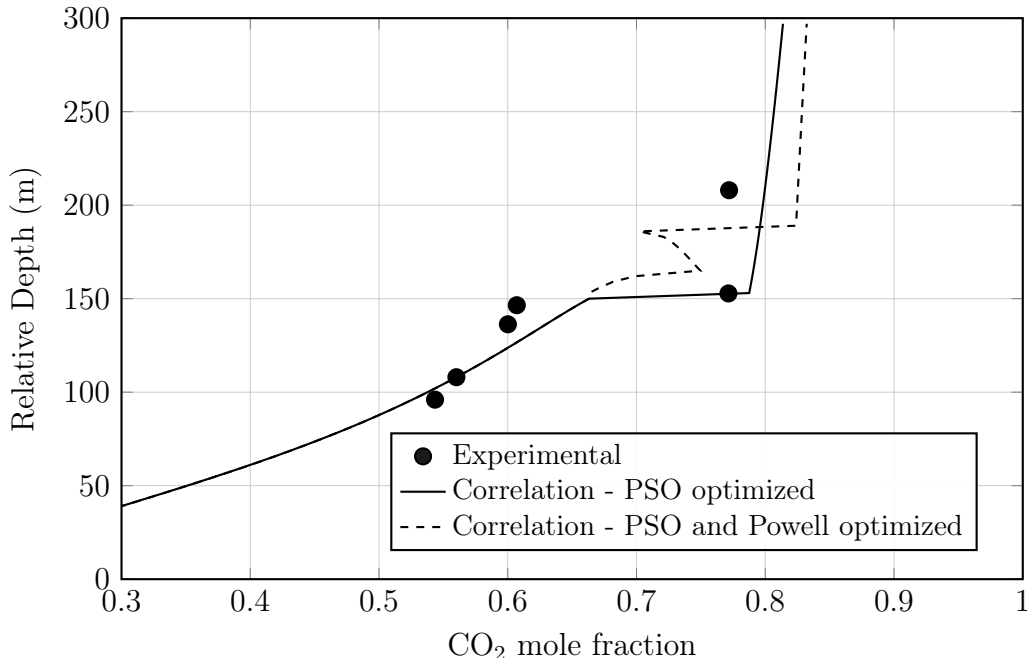


Figure 5.4: Comparison between CO₂ mole fraction profiles obtained with the PSO-optimized correlation with Powell refinement.

Table 5.2: Comparison of PSO and PSO plus Powell optimization results for the τ_{CO_2} correlation.

Optimization method	Objective function	$\alpha_0, \alpha_1, \beta_0, \beta_1$ parameters
PSO only	0.00611605	2.9211, 6.7964, -3.0324, 0.1147
PSO plus Powell	0.00610900	2.9215, 6.7964, -3.0324, 0.1147

Table 5.3 shows the root-mean-square error (RMSE) values for the cases tested. The RMSE was calculated over all points used in the objective function, corresponding to five pseudocomponent mole fractions at each of five depths (a total of 25 values). The correlation obtained through PSO achieved the lowest error, quantitatively confirming the trends observed in the profiles of Figure 5.3 and 5.4. The slightly higher RMSE for the Powell result reflects local numerical instabilities, reinforcing the choice of the PSO solution as the most consistent outcome.

To illustrate how the correlation behaves for other components, Figure 5.5 and 5.6 show the profiles for CH₄ and C₂₀₊. These plots are not used to assess accuracy, since all components are already included in the objective function. Instead, they

Table 5.3: Root-mean-square error (RMSE) between simulated and experimental CO_2 mole fractions for different τ_{CO_2} definitions.

Case	RMSE
$\tau_{\text{CO}_2} = 0.1$	0.0598
$\tau_{\text{CO}_2} = 0.15$	0.0673
$\tau_{\text{CO}_2} = 0.2$	0.0734
Isothermal	0.1370
PSO optimized	0.0296
PSO plus Powell optimized	0.0599

offer a visual check on the compositional trends. For CH_4 , the correlation follows the experimental profile more closely than the fixed value case ($\tau_{\text{CO}_2} = 0.1$). For C_{20+} , the differences are smaller, but the overall behavior is still better reproduced by the correlation.

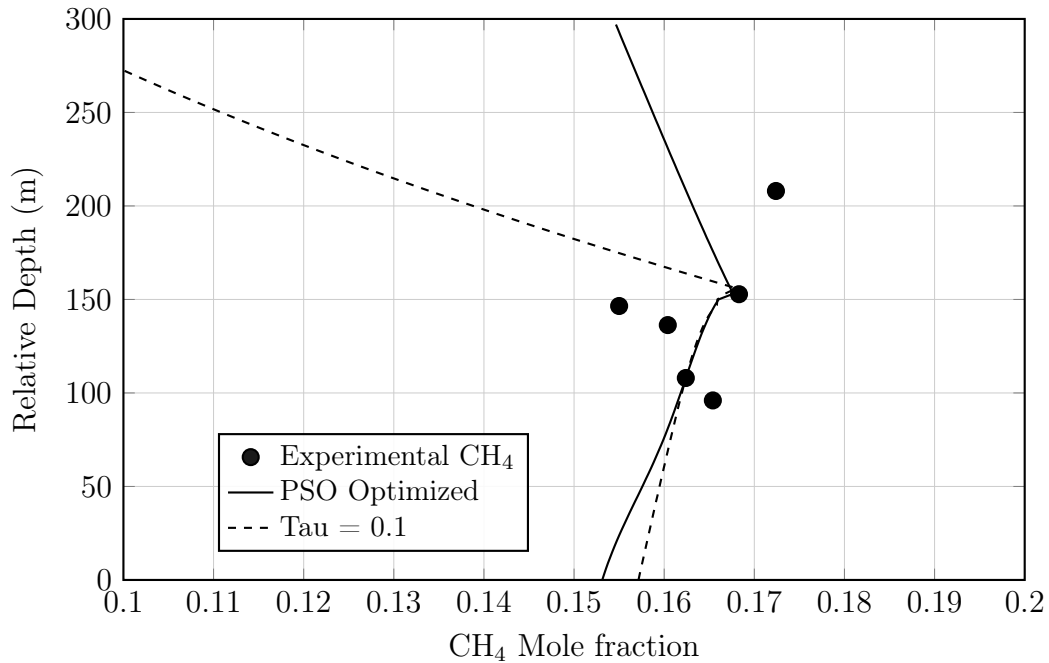


Figure 5.5: Comparison between experimental and simulated CH_4 mole fraction profiles for the PSO optimized correlation and the best fixed value case ($\tau_{\text{CO}_2} = 0.1$).

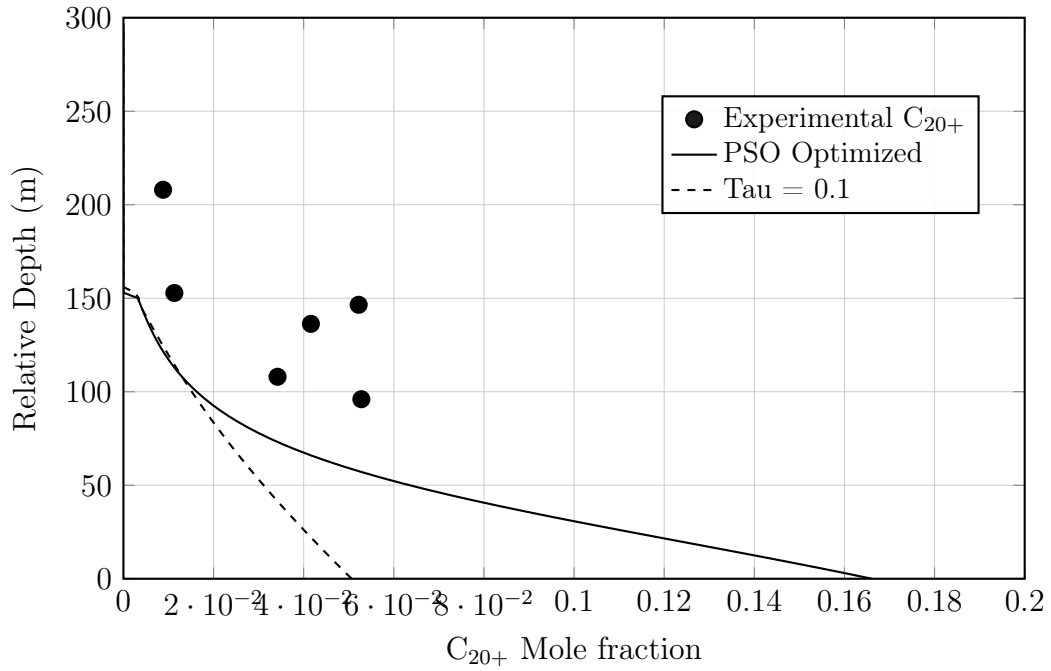


Figure 5.6: Comparison between experimental and simulated C_{20+} mole fraction profiles for the PSO optimized correlation and the best fixed value case ($\tau_{CO_2} = 0.1$).

To explore whether the optimized correlation could be used to define a fixed τ_{CO_2} , two tests used values taken directly from the correlation. The first applied the reference depth value ($\tau_{CO_2} = 0.6696$), representing the condition where PVT data were defined. The second considered a gas zone value ($\tau_{CO_2} = 0.0560$), which did not converge when applied. Therefore, the smallest value that converged was used ($\tau_{CO_2} = 0.0679$). The results are shown in Figure 5.7.

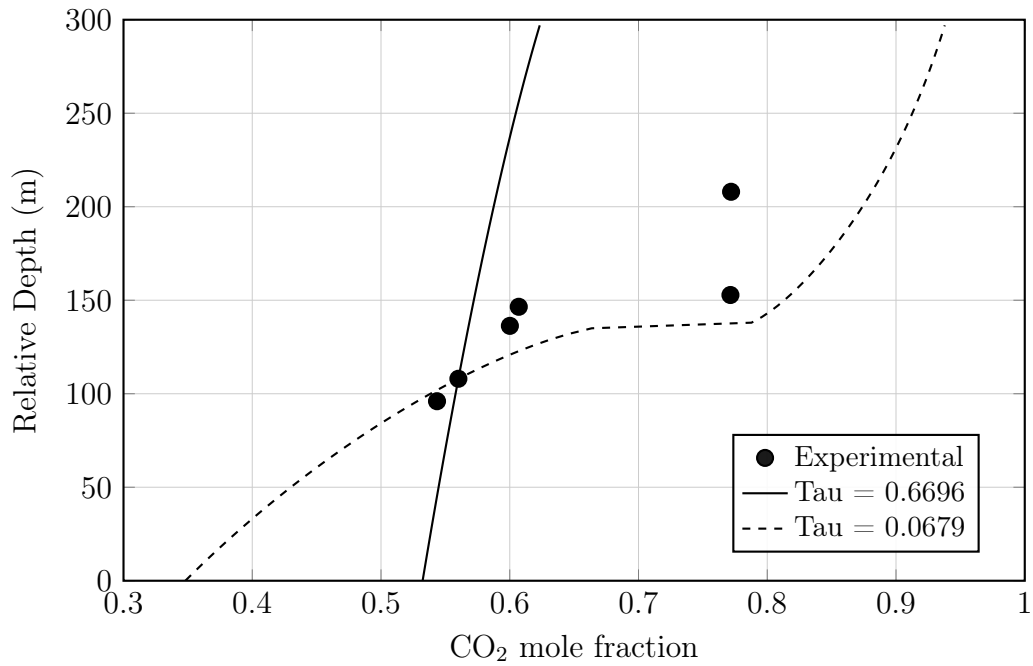


Figure 5.7: CO₂ mole fraction profiles using fixed values $\tau_{\text{CO}_2} = 0.6696$ and $\tau_{\text{CO}_2} = 0.0679$.

A second evaluation considered the values closer to the gas–oil contact. In this region, the correlation predicts $\tau_{\text{CO}_2} = 0.1591$ just below the contact and $\tau_{\text{CO}_2} = 0.1262$ just above it. As shown in Figure 5.8, these cases produced profiles that more closely resemble the best fixed-value tests performed manually.



Figure 5.8: CO₂ mole fraction profiles using fixed values $\tau_{\text{CO}_2} = 0.1262$ and $\tau_{\text{CO}_2} = 0.1591$.

Table 5.4 summarizes the RMSE values for the fixed cases and the optimized correlation. The fixed values taken near the gas–oil contact performed similarly to the best manual fixed test, while the PSO-optimized correlation provided the lowest error among the cases considered.

Table 5.4: RMSE comparison for the optimized correlation and selected fixed τ_{CO_2} values.

Case	τ_{CO_2} value	RMSE
PSO optimized correlation	(Table 5.1)	0.0296
Best manual fixed value	0.1	0.0598
Correlation at 136.3 m (above contact)	0.1262	0.0598
Correlation at 145.5 m (below contact)	0.1591	0.0732

These results complete the presentation of the τ_{CO_2} tests, which are further examined in the discussion.

5.1.1 Discussion

In the reservoir studied, characterized by high CO_2 content and the presence of a gas cap, the use of a depth–dependent τ_{CO_2} improved the match with measured compositional grading. As shown in Figure 5.3, the optimized correlation reproduced both the transition at the gas–oil contact and the steep profile in the gas zone, features that fixed values were not able to represent. Among the cases considered, the PSO–optimized formulation reached the lowest RMSE (Table 5.3) and provided a consistent description of the abrupt variation near the contact. The Powell refinement brought no meaningful gain, as illustrated in Figure 5.4 and Table 5.2, indicating that the PSO result was already close to optimal. In addition, the correlation did not compromise the fit of other components. Figure 5.5 and Figure 5.6 show that CH_4 and C_{20+} were reproduced at least as well as in the best fixed value case. Visually, the profiles follow the experimental trends with good agreement, while the objective function and RMSE already account for all components and depths simultaneously, indicating that the improvement reflects a global enhancement of the model rather than only the CO_2 profile.

Beyond this specific case, it is useful to consider how the role of τ_{CO_2} may vary under different reservoir conditions. In systems with lower CO_2 fractions, the influence of this parameter on compositional grading is expected to be less pronounced, and fixed values may still provide adequate predictions. Even in reservoirs with higher CO_2 content, the variation of τ_{CO_2} within the oil zone is relatively small, suggesting that in the absence of a gas cap, a fixed value could remain sufficient.

This makes the gas–oil contact the region where the distinction between fixed and variable approaches becomes most significant.

The relevance of the gas–oil contact is also reflected in the values of τ_{CO_2} listed in Table 5.1. Three distinct ranges appear: higher values in the oil zone (around 0.6–0.7), much lower values in the gas zone (close to 0.05), and intermediate values near the contact (0.1591 just below and 0.1262 just above). These differences are consistent with the contrasting compositional profiles across the phases, particularly the steep gradient in the gas zone. The ability of the correlation to vary across these conditions helps explain its advantage over fixed values, which cannot represent oil, contact, and gas regions simultaneously.

This variation arises from the dependence of τ_{CO_2} on the reduced temperature, defined as the ratio between the local reservoir temperature and the critical temperature of the mixture. Since the mixture’s critical temperature depends on composition, τ_{CO_2} indirectly varies with depth. The sharp transition observed at the contact reflects this relationship. As the fluid composition shifts from the oil phase to the gas phase, it becomes richer in light components. This change reduces the critical temperature, which in turn leads to smaller τ_{CO_2} values. In this sense, allowing the parameter to vary with depth provides a description that is more consistent with the observed profiles in this system.

The comparison between optimization methods also provides useful context. The PSO run consistently produced the lowest RMSE values and stable profiles, indicating that it was effective in identifying an adequate set of parameters for the correlation. The subsequent Powell refinement did not result in significant improvements, as seen in Figure 5.4 and Table 5.2. In some cases, small oscillations appeared near the gas zone, suggesting that the sensitivity observed in this region was more related to the simulator itself than to the optimizer. These results indicate that PSO alone was sufficient for this application, while Powell served mainly as a check rather than a necessary refinement.

Numerical instabilities were observed in some cases, particularly near the gas–oil transition and at the beginning of the gas zone. They appeared in the Powell refinement and in fixed–value runs with $\tau_{\text{CO}_2} \geq 0.2$, and became more evident for $\tau_{\text{CO}_2} = 0.5$ and higher. In the $\tau_{\text{CO}_2} = 0.1$ case, similar behavior could still be noticed, though in a much less pronounced way. These oscillations are not visible in some figures as they occur at depths outside the interval displayed, but their presence suggests a sensitivity of the simulator in that region. A likely explanation is related to the flash calculation routine, which may alternate between identifying the mixture as belonging to the oil region or to the gas region near the phase boundary. While the precise cause could not be fully determined, the fact that PSO did not produce such instabilities indicates that the heuristic search may have favored parameter sets

that are numerically more stable. This characteristic may have contributed to the good performance of the PSO-based correlation, in addition to the quality of the parameter adjustment itself.

Another aspect considered was whether the optimized correlation could assist in selecting a representative fixed τ_{CO_2} value, in situations where modifications to the simulator are not possible. As a first attempt, the value predicted at the reference depth ($\tau_{\text{CO}_2} = 0.6696$) was applied across the entire interval, since it corresponds to the conditions where the PVT data were defined. The result, however, did not reproduce the experimental trend or the gas-oil contact, as shown in Figure 5.7. A second test used a value from the gas zone. The correlation predicted a very small τ_{CO_2} (0.0560), but the simulator did not converge under this condition, so the lowest case that allowed convergence ($\tau_{\text{CO}_2} = 0.0679$) was considered. In this case as well, the agreement deteriorated mainly in the gas zone, remaining noticeably different from the experimental profile.

Since the values from the reference depth and from the gas zone did not perform well, further tests examined the correlation at depths immediately above and below the gas-oil contact, which gave intermediate values (0.1262 and 0.1591). As illustrated in Figure 5.8, these cases produced profiles more similar to the best fixed-value results obtained manually ($\tau_{\text{CO}_2} = 0.1$). The corresponding RMSE values in Table 5.4 confirm this observation, although none of the fixed cases reproduced the performance of the variable correlation, values near the contact aligned more closely with the experimental profiles than those taken from other depths. This indicates that, even if the correlation cannot be reduced to a single representative number, it may still provide a useful indication of the ranges where fixed values are more likely to perform adequately in cases where a gas-oil contact is present.

Overall, the results indicate that allowing τ_{CO_2} to vary with depth provides a more consistent description of compositional grading in reservoirs with high CO_2 content and a gas cap. The PSO-optimized correlation reproduced the transition at the gas-oil contact and the steep profile in the gas zone more effectively than any fixed value, while maintaining adequate predictions for other components. At the same time, the evaluation of fixed values derived from the correlation showed that, although no single value could match the performance of the variable formulation, the correlation still offered guidance for identifying ranges with better agreement, particularly near the contact. Taken together, these findings suggest that the choice between fixed and variable approaches should be made considering the reservoir characteristics, with variable τ_{CO_2} formulations providing clear advantages in systems where gas-oil transition and high CO_2 content play a significant role.

5.2 Results for Montel’s Modified Thermal Diffusion Model

This section presents the results obtained with Montel’s modified thermal diffusion model integrated into the simulator. For each field, simulated depth profiles are compared with those obtained using the formulations of FIROOZABADI *et al.* (2000), with $\tau_{C_i} = 4$ and $\tau_{CO_2} = 0.1$, and ESPÓSITO *et al.* (2017), also using $\tau_{CO_2} = 0.1$, all evaluated under the same reservoir simulator. Results based on the formulation of PEDERSEN and LINDELOFF (2003), generated using the software PVTsim version 7.1, are also included. In all cases, the isothermal scenario is shown as a baseline. The fitted L_i values for each pseudocomponent are reported together with the corresponding figures and tables for each field.

Unlike the previous analysis involving τ_{CO_2} , no adjustment of τ is performed here because Montel’s formulation does not include this parameter. In Firoozabadi’s model, thermal diffusion depends explicitly on the net heat of transport, which incorporates the parameter τ_i . In contrast, Montel’s model computes the heat of transport directly from the residual entropy, without relying on τ_i or on any associated correlations. Therefore, the refinement introduced in the earlier study has no direct analogue within Montel’s theoretical structure.

For this reason, the adjustable parameter adopted in Montel’s modified formulation is the Onsager coefficient L_i , treated as a depth-independent constant for each pseudocomponent. This choice allows a controlled simplification while remaining consistent with the structure of the model, and provides a practical way to evaluate whether Montel’s framework can reproduce measured compositional gradients.

5.2.1 Field A

Field A corresponds to the reproduction of the case based on NEMD simulations presented by MONTEL *et al.* (2019) and BAGHOOEE *et al.* (2021). The available dataset includes depth profiles for the lighter components N_2-C_1 and CO_2 , and for the heavier components CN1 and CN2. All these components data were considered in the optimization.

Figures Figure 5.9–Figure 5.12 show the simulated depth profiles of N_2-C_1 , CO_2 , CN1, and CN2. The curves obtained with Montel’s modified formulation are presented alongside those from the formulations of FIROOZABADI *et al.* (2000) and ESPÓSITO *et al.* (2017), with the isothermal reference included for comparison.

The simulated profiles obtained with Montel’s modified formulation show good visual agreement with the reference data for both lighter and heavier components. The curves reproduce the observed gradients within the tested range, even with

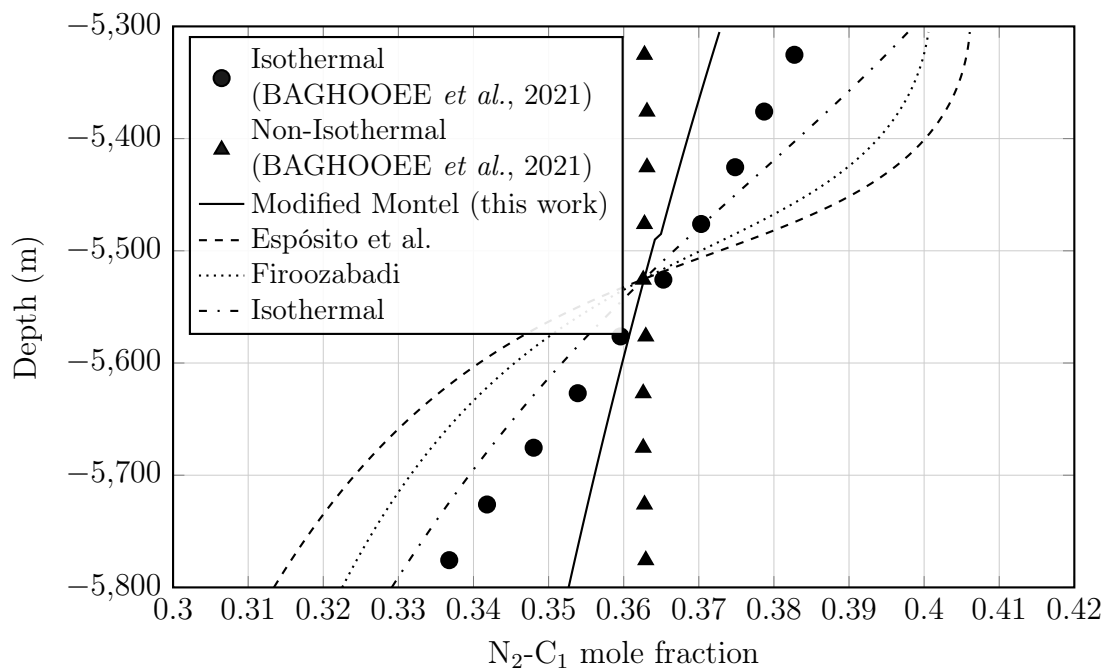


Figure 5.9: Simulated mole fraction profiles for N_2-C_1 in Field A using Montel's modified thermal diffusion formulation, compared with alternative models.

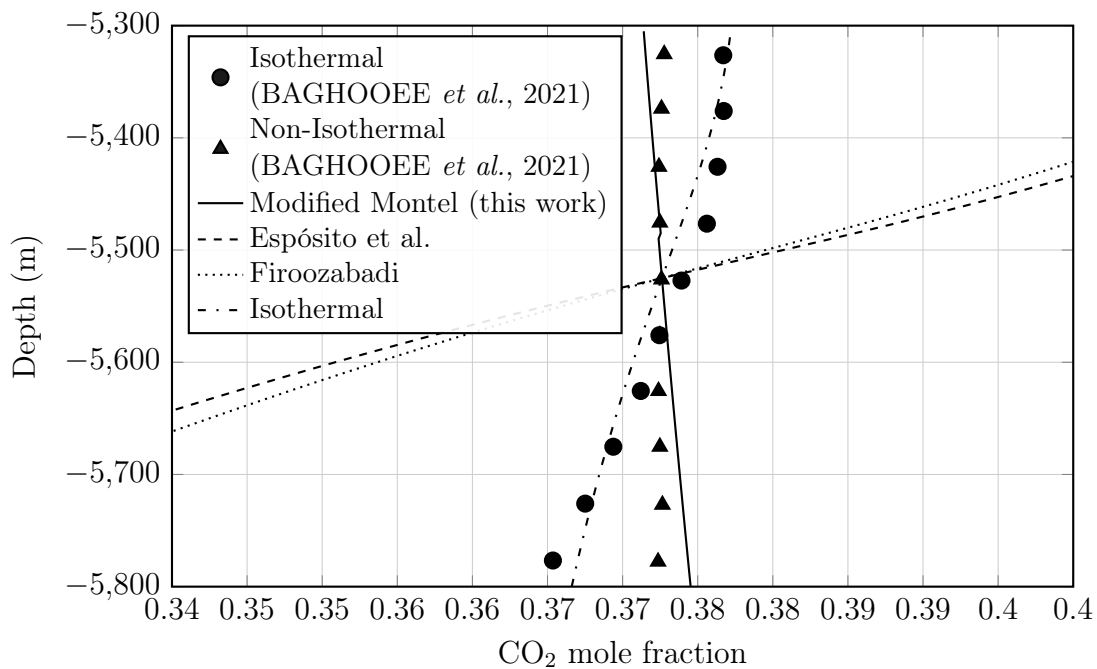


Figure 5.10: Simulated mole fraction profiles for CO_2 in Field A using Montel's modified thermal diffusion formulation, compared with alternative models.

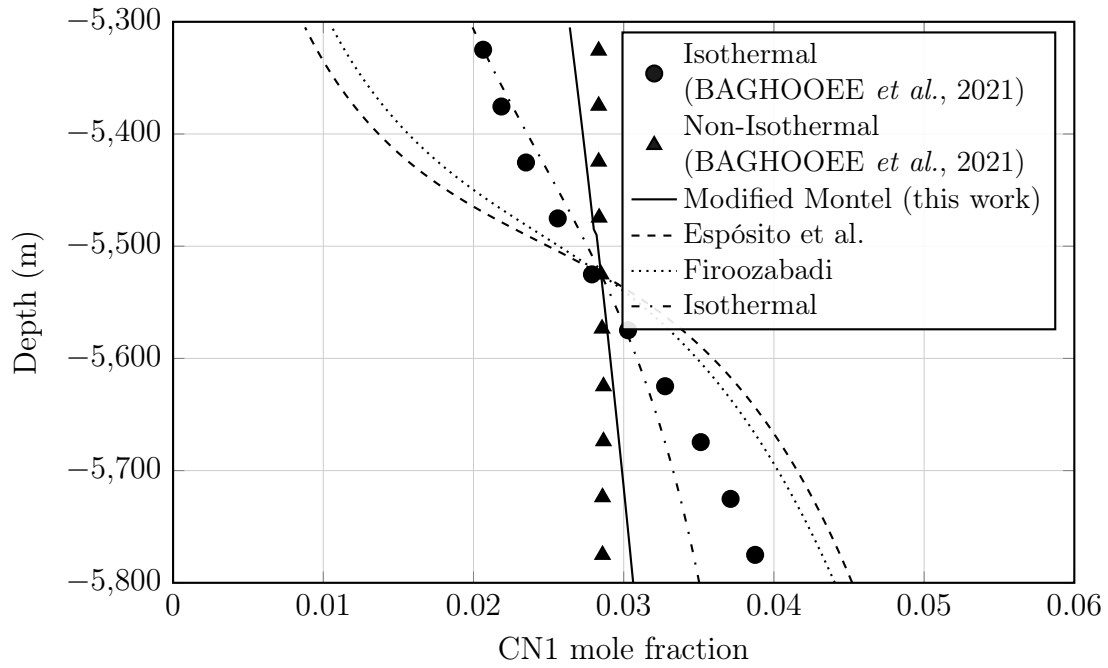


Figure 5.11: Simulated mole fraction profiles for CN1 in Field A using Montel’s modified thermal diffusion formulation, compared with alternative models.

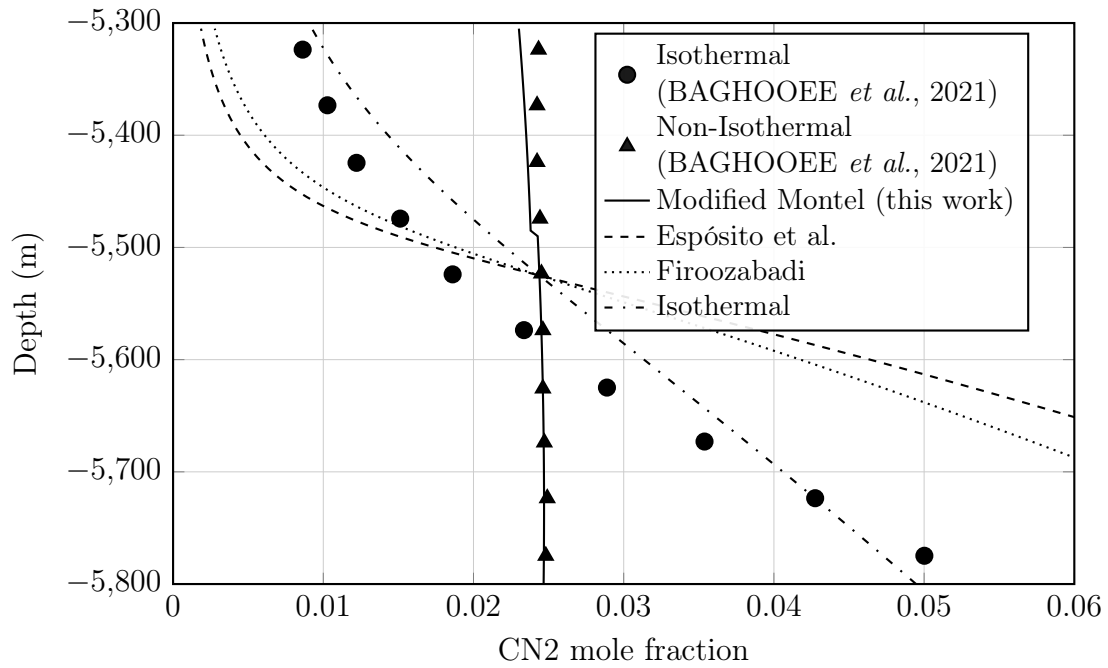


Figure 5.12: Simulated mole fraction profiles for CN2 in Field A using Montel’s modified thermal diffusion formulation, compared with alternative models.

constant L_i values along the column.

The fitted L_i values for Field A are listed in Table 5.5. These correspond to the parameters adjusted for each pseudocomponent and were applied uniformly along the depth column.

Table 5.5: Transport coefficients L_i fitted for Field A.

PComp.	L_i
N ₂ -C ₁	3.24×10^{-13}
CO ₂	1.45×10^{-10}
C ₂	5.23×10^{-11}
C ₃ -C ₄	1.37×10^{-08}
C ₅ -C ₁₀	1.07×10^{-11}
C ₁₁ -C ₁₉	4.71×10^{-13}
CN1	1.04×10^{-13}
CN2	9.91×10^{-14}

The root mean square error (RMSE) for Field A, comparing the different formulations, is reported in Table 5.6.

Table 5.6: RMSE values for Field A considering each thermal diffusion formulation.

Model	RMSE
Firoozabadi	0.0278
Esp3sito et al.	0.0326
Isothermal	0.0130
Modified Montel (this work)	0.0032

5.2.2 Field B

Field B contains data from a single well. The reference sample corresponds to oil collected at 93 m, and the target sample at 351 m. These data were used in the optimization, with L_i values treated as constant, as in Field A.

Figure 5.13 and Figure 5.14 present the simulated mole fraction profiles for N₂-C₁ and C₂₀₊ in Field B, obtained with Montel’s modified thermal diffusion formulation. The results are shown together with the experimental reference and the alternative models.

For N₂-C₁ (Figure 5.13), the models reproduce the compositional trend with small variations in the predicted gas-oil contact depth. For C₂₀₊ (Figure 5.14), the simulated profiles are also similar across the formulations, with only minor differences along the column.

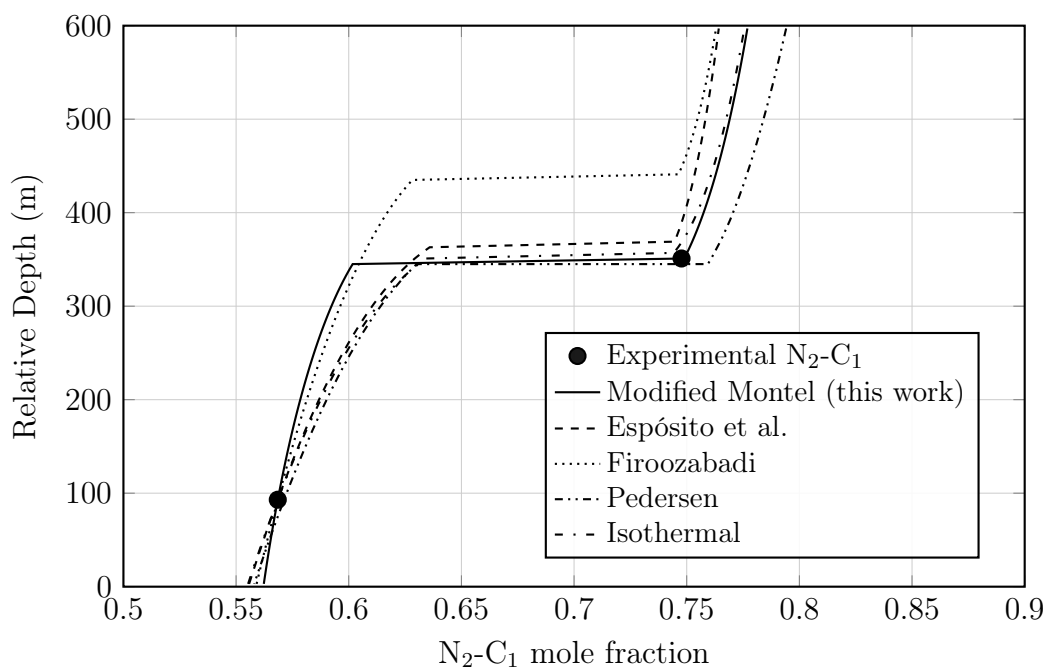


Figure 5.13: Simulated and measured mole fraction profiles for N_2-C_1 in Field B using Montel's modified thermal diffusion formulation, compared with alternative models.

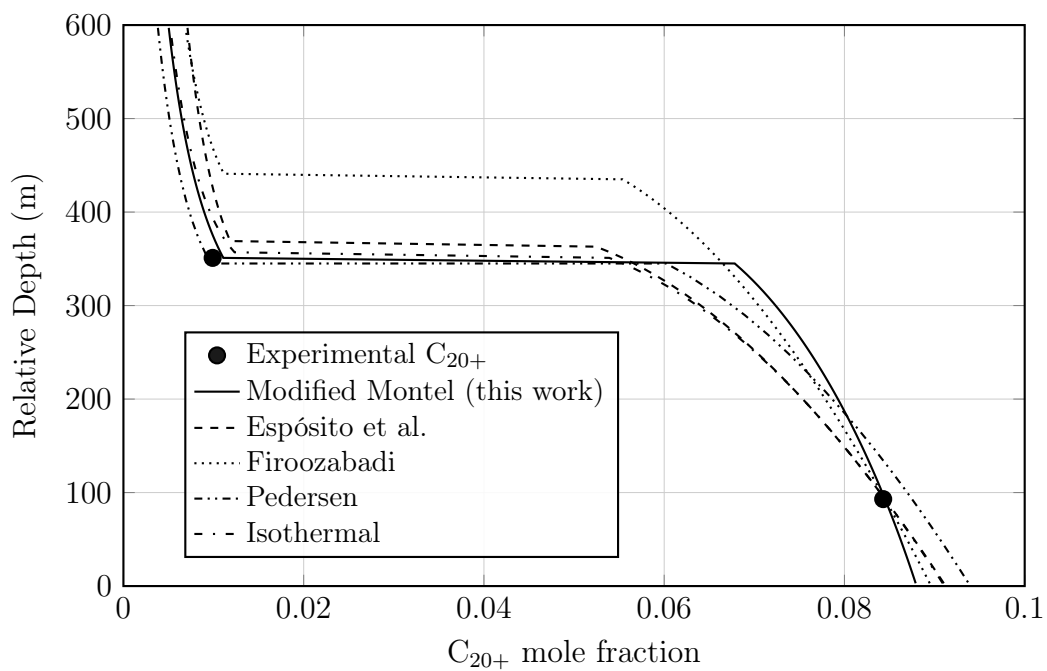


Figure 5.14: Simulated and measured mole fraction profiles for C_{20+} in Field B using Montel's modified thermal diffusion formulation, compared with alternative models.

The optimized L_i values for each pseudocomponent are listed in Table 5.7.

Table 5.7: Optimized L_i values for each pseudocomponent in Field B using Montel’s modified thermal diffusion formulation.

PComp.	L_i (mol K s/kg)
CO ₂	1.1325×10^{-12}
N ₂ -C ₁	1.0000×10^{-12}
C ₂ -C ₅	4.8592×10^{-12}
C ₆ -C ₁₂	1.0000×10^{-12}
C ₁₃ -C ₁₉	1.1004×10^{-12}
QC24	1.0000×10^{-12}
QC43	4.4920×10^{-10}
QC70	2.6130×10^{-8}

The root mean square error (RMSE) for Field B, comparing all formulations, is reported in Table 5.8.

Table 5.8: RMSE values for Field B considering each thermal diffusion formulation.

Model	RMSE
Firoozabadi	0.0657
Esp3sposito et al.	0.0547
Pedersen	0.0683
Isothermal	0.0526
Modified Montel (this work)	0.0100

5.2.3 Field C

Field C uses data from three wells. Well 1 provided uncontaminated production test samples, while Wells 2 and 3 contributed with bottom-hole samples. The reference point was taken from Well 1, with the remaining samples included in the objective function. Simulated profiles obtained with the Montel’s modified formulation are compared with those from the models of FIROOZABADI *et al.* (2000) and ESP3SPOSITO *et al.* (2017). No results were generated for Pedersen’s formulation in this case.

Figure 5.15 and Figure 5.16 show the experimental data alongside the simulated curves for N₂-C₁ and C₂₀₊. The profiles indicate that the models reproduce the overall compositional trends, with visible differences in the predicted gradients along the column.

The optimized L_i values obtained for Field C are listed in Table 5.9. These values were applied as constant parameters for each pseudocomponent in the simulations.

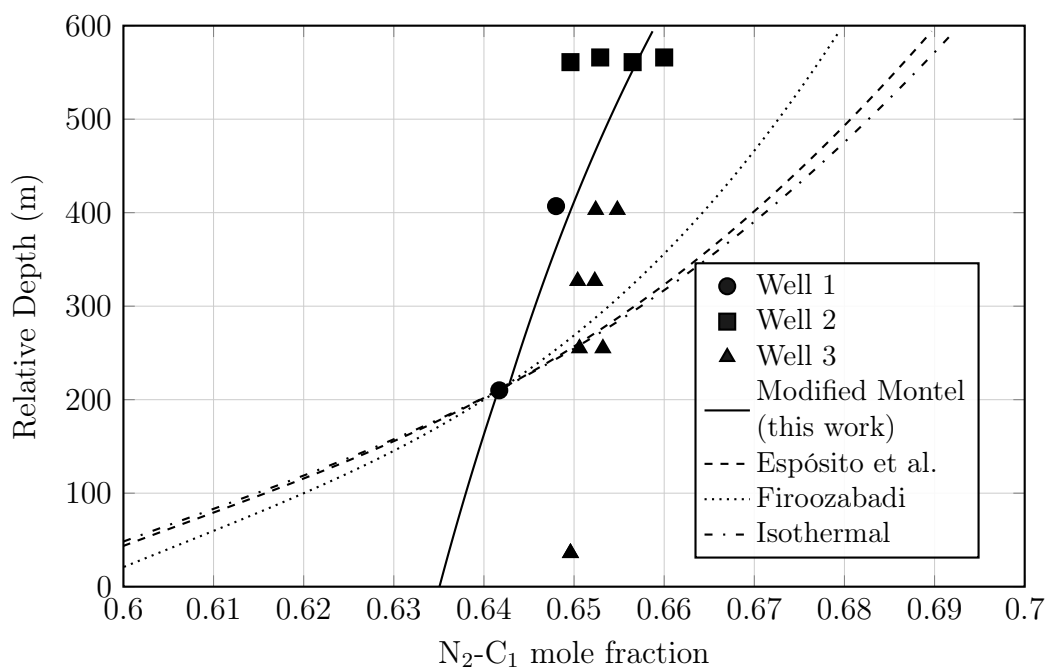


Figure 5.15: Simulated and measured mole fraction profiles for N_2-C_1 in Field C using Montel's modified thermal diffusion formulation, compared with alternative models.

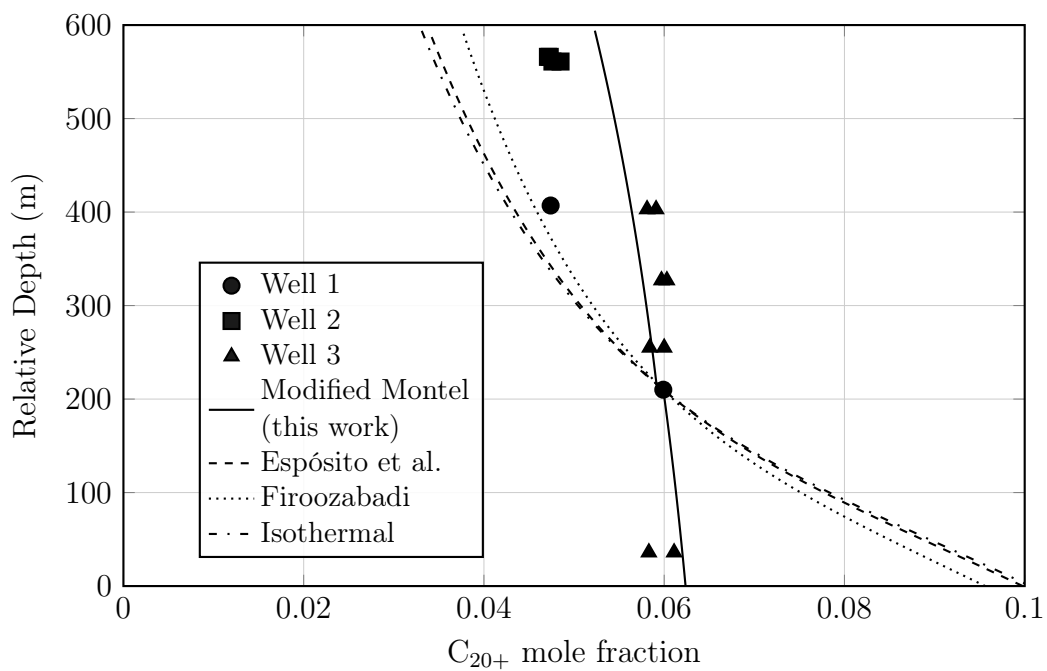


Figure 5.16: Simulated and measured mole fraction profiles for C_{20+} in Field C using Montel's modified thermal diffusion formulation, compared with alternative models.

Table 5.9: Optimized L_i values for each pseudocomponent in Field C.

PComp.	L_i
CO ₂	2.3051×10^{-11}
N ₂ -C ₁	3.5963×10^{-11}
C ₂	7.1273×10^{-11}
C ₃ -C ₄	1.5517×10^{-11}
C ₅ -C ₁₂	1.2899×10^{-11}
C ₁₃ -C ₁₉	5.5980×10^{-11}
QC26	2.1337×10^{-11}
QC57	5.8845×10^{-12}

The root mean square error (RMSE) values for Field C, comparing the different formulations, are given in Table 5.10.

Table 5.10: RMSE values for Field C considering each thermal diffusion formulation.

Model	RMSE
Firoozabadi	0.0176
Esp3sito et al.	0.0217
Isothermal	0.0227
Modified Montel (this work)	0.0055

5.2.4 Discussion

The three reservoir cases analyzed cover distinct conditions, ranging from simulated fluids to real production data. This diversity provides a broader view of how Montel’s modified formulation behaves under different contexts.

For Field A, the dataset from NEMD simulations allowed a first application of the modified Montel formulation. The simulated profiles reproduced the reference data with good agreement for all components. In Figure 5.9 and Figure 5.10, which show the lighter fractions N₂-C₁ and CO₂, the model captured the experimental trends while producing a less pronounced gradient along the column. A similar effect was observed for the heavier components, CN1 and CN2 (Figure 5.11 and Figure 5.12). Across all four cases, Montel’s modified model consistently attenuated the compositional grading when compared with the isothermal reference. By contrast, the formulations of Firoozabadi and Esp3sito et al. tended to intensify the gradients relative to the isothermal case. This consistent behavior across light and heavy components indicates that the assumption of constant L_i with depth was not only numerically stable but also effective in reproducing the experimental trends in

this case.

In Field B, the dataset was restricted to two depth points, with an oil sample at 93 m and a gas sample at 351 m. This makes the definition of the gas–oil contact especially relevant. The simulated profiles obtained with Montel’s modified formulation followed the same overall trend as the alternative models, with all of them placing the gas–oil contact at similar depths. The main distinction is that Montel’s model predicted a stronger contrast between the oil and gas phase compositions. This can be observed in the N_2-C_1 results (Figure 5.13), where the difference between the phases was more pronounced than in the other models. A similar effect is present in the heavier fractions, particularly C_{20+} (Figure 5.14), where the profile reproduced the experimental points near the reference depth while accentuating the separation between phases along the column.

In Field C, which combines samples from three wells, Montel’s modified formulation provided the closest match to the experimental data among the tested models. For N_2-C_1 (Figure 5.15), the model produced a steeper profile than the alternatives, following the measured points across the column more closely. For C_{20+} (Figure 5.16), the simulated curve reproduced the experimental values near the reference depth and maintained good agreement toward the top. Compared with the Firoozabadi and Espósito et al. models, Montel’s modified formulation introduced a distinct curvature that presents a visually good alignment with the available data. This agreement is also reflected in the RMSE values (Table 5.10), where Montel’s modified model achieved the lowest error among the tested formulations. As in Field A, the model shows a tendency to attenuate the compositional grading. In this case, however, the same attenuating behavior is also observed in the other formulations.

An important aspect of Field C is the quality and consistency of the experimental data itself. Well 2 includes two samples collected at nearby depths, and the spread between them is visible in the plotted profiles. For N_2-C_1 , the samples from Well 1 appear to follow a different trend compared with Wells 2 and 3, making it possible to imagine two distinct lines of best fit across the dataset. It is not straightforward to determine which set of points is more reliable. Wells 2 and 3 provide bottom-hole samples that may be affected by contamination, while the samples from Well 1 are uncontaminated but were taken during production from a perforated interval. Using the midpoint of this interval as the representative depth is a practical approximation considering a uniform inflow across the open section, which is not necessarily true. These factors highlight that numerical error values should not be interpreted by itself, and the fit must be judged in light of the experimental uncertainties.

When considered together, the three cases show consistent patterns in the behavior of Montel’s modified formulation. In Field A, the model tended to attenuate the compositional grading compared with the isothermal reference, in contrast to

the Firoozabadi and Espósito et al. formulations, which amplified it. In Field B, the results of all models were similar, since the field was already well described by the isothermal case. Still, Montel’s approach matched the depth of the gas–oil contact more closely and again showed the same attenuating behaviour. In Field C, where the dataset was larger and more diverse, Montel’s modified formulation gave the closest overall match to the experimental data and the lowest RMSE. Across these different reservoir conditions, the model showed a consistent tendency to moderate the compositional gradient.

Regarding the fitted L_i values, Field B showed a tendency for higher values in the heavier fractions, while in Fields A and C no clear trend was observed across the pseudocomponents. The order of magnitude remained similar among all fields, indicating consistency in the optimization process. Field B behaved close to the isothermal case despite its L_i distribution, suggesting that the coefficients are not the main factor controlling the strength of the temperature gradient effect.

This interpretation is consistent with the RMSE values obtained across the three fields (Table 5.6, Table 5.8, and Table 5.10), where Montel’s modified formulation provided the lowest error in every case. Together with the visual inspection of the profiles, these results confirm that the modified formulation not only achieves numerical improvements but also reproduces the depth-dependent trends in a way that remains consistent across distinct reservoir conditions.

Overall, the results indicate that Montel’s modified formulation is able to reproduce compositional grading across a variety of reservoir conditions, from synthetic cases to more complex field datasets. The hypothesis of treating L_i as an adjustable but depth-independent parameter for each pseudocomponent proved effective, since it allowed the model to capture the observed gradients while keeping a consistent behavior across all cases.

Chapter 6

Conclusion

This work examined how targeted refinements to existing thermal-diffusion formulations can improve the description of compositional grading in hydrocarbon reservoirs. The central objective was to evaluate whether adjustments to model parameters and assumptions could bring simulated profiles closer to measured data while maintaining thermodynamic consistency.

The first part of the study focused on Firoozabadi’s formulation, with particular attention to the thermal diffusion coefficient and parameter τ_{CO_2} . Although correlations were already available for hydrocarbons components, no equivalent expression existed for CO_2 . Extending the correlation proposed by ESPÓBITO *et al.* (2017) to CO_2 and allowing τ_{CO_2} to vary with depth improved the agreement in a CO_2 rich reservoir, especially near the gas–oil contact and within the gas zone.

The second part evaluated a modified version of Montel’s formulation in which the Onsager coefficients L_i were treated as adjustable but constant with depth. The goal was to verify whether this simplified assumption could still capture reservoir-scale compositional variations. Across three datasets of increasing complexity, including both synthetic and real fields, the modified formulation produced stable solutions and followed the measured data with good agreement. The results consistently showed a tendency to attenuate the compositional gradient relative to the isothermal reference, while still reproducing the overall behavior expected from the field observations.

Considering both approaches, the results indicate that incremental refinements can make thermal diffusion models more reliable without altering their theoretical structure. Extending the correlation for τ_{CO_2} provided consistent improvements in CO_2 rich systems, and the modified Montel approach demonstrated that using adjustable, depth-independent L_i values can effectively reproduce compositional profiles across distinct reservoir settings.

It is important to interpret these improvements in light of the available data. Although explicit estimates of experimental uncertainty were not provided for the

compositional measurements, these data represent the best information currently accessible for the analyzed reservoirs. Within this context, the reductions in RMSE observed across the cases constitute a consistent indication that the proposed modifications enhance the match with measured profiles under the examined conditions. Still, without quantified uncertainty bounds, the exact magnitude of these improvements cannot be fully assessed. A more detailed evaluation of how measurement variability affects model discrimination remains an important direction for future work.

The conclusions of this study are inherently bounded by the number of cases analyzed and by the one-dimensional simulation setup adopted. Future developments could extend the analysis to two or three dimensional simulations, explore new correlations for τ_{CO_2} , and investigate whether the Onsager coefficients vary with depth or composition. Applying these ideas to more complex scenarios would help evaluate where the modifications proposed here remain effective and where new adjustments are required.

A more balanced comparison across models would also require calibrating the adjustable parameters in the formulations of Firoozabadi and Espósito, which in this work were used with the standard literature values. Optimizing these parameters was not pursued here, as it lies outside the scope of the present study, whose focus was to investigate the proposed modifications to the selected thermal-diffusion models. Even so, performing such calibration in future work would be valuable to enable a fairer assessment of the relative performance of the different formulations.

Overall, the study shows that progress in modeling compositional grading can come from incremental refinements to existing formulations. Allowing τ_{CO_2} to vary with depth and treating L_i as adjustable parameters brought the models closer to field data while preserving their theoretical consistency. These approaches do not solve all aspects of compositional grading, but they indicate that gradual improvements, supported by systematic testing, can make reservoir models more robust.

References

- BAGHOOEE, H., MONTEL, F., GALLIERO, G., YAN, W., SHAPIRO, A., 2021, “A new approach to thermal segregation in petroleum reservoirs: Algorithm and case studies”, *Journal of Petroleum Science and Engineering*, v. 201, pp. 108367. doi: 10.1016/j.petrol.2021.108367.
- CALSEP A/S, 2022, *PVTsim Nova 2022*. Calsep. Compositional PVT Analysis and Equation of State Modeling Software.
- COMPUTER MODELLING GROUP LTD., 2022, *WinProp: PVT and phase behaviour modeling software*. CMG, Calgary. Version 2022.10.
- CREEK, J. L., SCHRADER, M. L., 1985, “East Painter Reservoir: an example of a compositional gradient from a gravitational field”. In: *SPE Annual Technical Conference and Exhibition*, Las Vegas, Nevada. Society of Petroleum Engineers. doi: 10.2118/14411-MS.
- DAKE, L. P., 1978, *Fundamentals of Reservoir Engineering*. Amsterdam, Elsevier. ISBN: 978-0-444-41830-2.
- DANESH, A., 1998, *PVT and Phase Behaviour of Petroleum Reservoir Fluids*. Amsterdam, Elsevier. ISBN: 0-444-82196-1.
- DE GROOT, S. R., MAZUR, P., 1984, *Non-Equilibrium Thermodynamics*. New York, NY, Dover Publications. ISBN: 978-0-486-64741-8.
- DONG, C., ELSHAHAWI, H., MULLINS, O. C., VENKATARAMANAN, L., HOWS, M., MCKINNEY, D., FLANNERY, M., HASHEM, M., 2007, “Improved interpretation of reservoir architecture and fluid contacts through the integration of downhole fluid analysis with geochemical and mud gas analyses”. In: *Proceedings of the Asia Pacific Oil and Gas Conference and Exhibition*, Jakarta, Indonesia. Society of Petroleum Engineers. doi: 10.2118/109683-MS.

- DOUGHERTY JR., E. L., DRICKAMER, H. G., 1955, “A theory of thermal diffusion in liquids”, *The Journal of Chemical Physics*, v. 23, n. 2, pp. 295–309. doi: 10.1063/1.1741957.
- ENGLAND, W. A., MACKENZIE, A. S., MANN, D. M., QUIGLEY, T. M., 1987, “The movement and entrapment of petroleum fluids in the subsurface”, *Journal of the Geological Society*, v. 144, n. 2, pp. 327–347. doi: 10.1144/gsjgs.144.2.0327.
- ESPÓSITO, R. O., ALIJÓ, P. H. R., SCILIPOTI, J. A., TAVARES, F. W., 2017, *Compositional Grading in Oil and Gas Reservoirs*. Cambridge, MA, Gulf Professional Publishing, Elsevier. ISBN: 978-0-12-812452-9.
- FIROOZABADI, A., 1999, *Thermodynamics of Hydrocarbon Reservoirs*. New York, NY, McGraw-Hill. ISBN: 978-0-07-022071-3.
- FIROOZABADI, A., 2016, *Thermodynamics and Application in Hydrocarbon Energy Production*. New York, NY, McGraw-Hill. ISBN: 978-0-07-184330-0.
- FIROOZABADI, A., GHORAYEB, K., SHUKLA, K., 2000, “Theoretical model of thermal diffusion factors in multicomponent mixtures”, *AIChE Journal*, v. 46, n. 5, pp. 892–900. doi: 10.1002/aic.690460504.
- GHORAYEB, K., ANRAKU, T., FIROOZABADI, A., 2000, “Interpretation of the fluid distribution and GOR behavior in the Yufutsu fractured gas-condensate field”. In: *SPE Asia Pacific Conference on Integrated Modelling for Asset Management*, Yokohama, Japan. Society of Petroleum Engineers. doi: 10.2118/59437-MS.
- GHORAYEB, K., FIROOZABADI, A., 2000a, “Molecular, pressure, and thermal diffusion in nonideal multicomponent mixtures”, *AIChE Journal*, v. 46, n. 5, pp. 883–891. doi: 10.1002/aic.690460503.
- GHORAYEB, K., FIROOZABADI, A., 2000b, “Modeling multicomponent diffusion and convection in porous media”, *SPE Journal*, v. 5, n. 2, pp. 158–171. doi: 10.2118/62168-PA.
- GO, J., SMALLEY, P. C., MUGGERIDGE, A., 2012, “Appraisal of reservoir compartmentalization using fluid mixing time-scales: Horn Mountain Field, Gulf of Mexico”, *Petroleum Geoscience*, v. 18, n. 3, pp. 305–314. doi: 10.1144/1354-079311-079.
- HAASE, R., 1969, *Thermodynamics of Irreversible Processes*. London, Addison-Wesley.

- KATZ, D. L., FIROOZABADI, A., 1978, “Predicting phase behavior of condensate/crude-oil systems using methane interaction coefficients”, *Journal of Petroleum Technology*, v. 30, n. 11, pp. 1649–1655. doi: 10.2118/6721-PA.
- LIRA-GALEANA, C., FIROOZABADI, A., PRAUSNITZ, J. M., 1994, “Computation of compositional grading in hydrocarbon reservoirs. Application of continuous thermodynamics”, *Fluid Phase Equilibria*, v. 102, n. 2, pp. 143–158. doi: 10.1016/0378-3812(94)87073-X.
- LOURENÇO, E., VIEIRA, A. J. M., CAMARGO, G. M., FERREIRA, L. P., ALLEBRANDT, C., 2016, “Influência da contaminação por filtrado de perfuração sintético em óleos leves”. In: *Rio Oil & Gas Expo and Conference Proceedings*, Rio de Janeiro, Brasil. Instituto Brasileiro de Petróleo, Gás e Biocombustíveis (IBP). IBP2030_16. Available at: IBP Digital Library.
- MONTEL, F., GOUEL, P. L., 1985, “Prediction of compositional grading in a reservoir fluid column”. In: *SPE Annual Technical Conference and Exhibition*, Las Vegas, Nevada. Society of Petroleum Engineers. doi: 10.2118/14410-MS.
- MONTEL, F., HOANG, H., GALLIERO, G., 2019, “Linking up pressure, chemical potential and thermal gradients”, *The European Physical Journal E*, v. 42, n. 5, pp. 65. doi: 10.1140/epje/i2019-11821-0.
- OKOH, O. M., LAWAL, K. A., YADUA, A. U., ODUDE, A., ANYANWU, O. T., OVURU, M. I., EYITAYO, S. I., PELEMO, B., AKEWUSOLA, T., MATEMILOLA, S., RAMASWAMY, S., NWAERI, E., 2020, “Using limited and cheap PVT data to reduce GOC uncertainties in reservoirs with unknown GOC”. In: *SPE Nigeria Annual International Conference and Exhibition*, Virtual. Society of Petroleum Engineers. doi: 10.2118/203611-MS.
- OPENAI, 2025. “ChatGPT: GPT-4 model”. Accessed in September 2025. Available at: <https://chat.openai.com>.
- PEDERSEN, K. S., LINDELOFF, N., 2003, “Simulations of compositional gradients in hydrocarbon reservoirs under the influence of a temperature gradient”. In: *SPE Annual Technical Conference and Exhibition*, Denver, Colorado. Society of Petroleum Engineers. doi: 10.2118/84364-MS.

- PETERS, K. E., FOWLER, M. G., 2002, “Applications of petroleum geochemistry to exploration and reservoir management”, *Organic Geochemistry*, v. 33, n. 1, pp. 5–36. doi: 10.1016/S0146-6380(01)00125-5.
- RAHMAN, M. A., SAGUIR, M. Z., 2014, “Thermodiffusion or Soret effect: historical review”, *International Journal of Heat and Mass Transfer*, v. 73, pp. 693–705. doi: 10.1016/j.ijheatmasstransfer.2014.02.057.
- RILEY, M. F., FIROOZABADI, A., 1998, “Compositional variation in hydrocarbon reservoirs with natural convection and diffusion”, *AIChE Journal*, v. 44, n. 2, pp. 452–464. doi: 10.1002/aic.690440221.
- ROSA, A. J., DE S. CARVALHO, R., XAVIER, J. A. D., 2006, *Engenharia de Reservatórios de Petróleo*. Rio de Janeiro, Interciência. ISBN: 978-8571931350.
- SCHULTE, A. M., 1980, “Compositional variations within a hydrocarbon column due to gravity”. In: *SPE Annual Technical Conference and Exhibition*, Dallas, Texas. Society of Petroleum Engineers. doi: 10.2118/9235-MS.
- SERRA, O., 2008, *Well Logging Handbook*. Paris, Editions Technip. ISBN: 978-2710809128.
- SHAIKH, J. A., MURATA, K., KURAMATA, H., MOGENSEN, H. K., 2024, “Impact of a vertical temperature gradient on H₂S gradient in sour, near-critical reservoir fluids”. In: *SPE Conference at Oman Petroleum & Energy Show*, Muscat, Oman. Society of Petroleum Engineers. doi: 10.2118/218801-MS.
- SHIBATA, S. K., SANDLER, S. I., BEHRENS, R. A., 1987, “Phase equilibrium calculations for continuous and semicontinuous mixtures”, *Chemical Engineering Science*, v. 42, n. 8, pp. 1977–1988. doi: 10.1016/0009-2509(87)80144-6.
- SHUKLA, K., FIROOZABADI, A., 1998, “A new model of thermal diffusion coefficients in binary hydrocarbon mixtures”, *Industrial & Engineering Chemistry Research*, v. 37, n. 8, pp. 3331–3342. doi: 10.1021/ie970896p.
- SMALLEY, P. C., ENGLAND, W. A., 1994, “Reservoir compartmentalization assessed with fluid compositional data”, *SPE Reservoir Engineering*, v. 9, n. 03, pp. 175–180. doi: 10.2118/25005-PA.

- THOMPSON, K. F. M., 1987, “Fractionated aromatic petroleums and the generation of gas-condensates”, *Organic Geochemistry*, v. 11, n. 6, pp. 573–590. doi: 10.1016/0146-6380(87)90011-8.
- VINHAL, A., AZEEM, J., PEDERSEN, K., 2021, “Modeling of compositional grading in heavy oil fields”. In: *SPE Annual Technical Conference and Exhibition*, Dubai, UAE. Society of Petroleum Engineers. doi: 10.2118/205887-MS.
- WHEATON, R. J., 1991, “Treatment of variations of composition with depth in gas-condensate reservoirs”, *SPE Reservoir Engineering*, v. 6, n. 2, pp. 239–244. doi: 10.2118/18267-PA.
- WHITSON, C. H., 1983, “Characterizing hydrocarbon plus fractions”, *Society of Petroleum Engineers Journal*, v. 23, n. 4, pp. 683–694. doi: 10.2118/12233-PA.
- WHITSON, C. H., BRULÉ, M. R., 2000, *Phase Behavior*. Richardson, TX, Society of Petroleum Engineers. ISBN: 978-1-55563-087-4.

Appendix A

Detailed Entropy Balance Derivation

This appendix presents the detailed derivation of the local entropy production expression in Equation 2.36, starting from the entropy balance (2.30) and the entropy flux definition (2.32).

Expanding the time derivative of (ρs) using the product rule, the first term becomes:

$$\frac{\partial(\rho s)}{\partial t} = \rho \frac{\partial s}{\partial t} - \rho s (\nabla \cdot \mathbf{v}) \quad (\text{A.1})$$

The entropy balance equation is then written as:

$$\rho \frac{\partial s}{\partial t} = -\nabla \cdot \mathbf{J}_s + \rho s (\nabla \cdot \mathbf{v}) + \sigma \quad (\text{A.2})$$

Grouping the terms inside the divergence operator:

$$\rho \frac{\partial s}{\partial t} = -\nabla \cdot (\mathbf{J}_s - \rho s \mathbf{v}) + \sigma \quad (\text{A.3})$$

Substituting Equation 2.32 into Equation A.3:

$$\rho \frac{\partial s}{\partial t} = -\nabla \cdot \left(\frac{\mathbf{J}_q}{T} - \sum_{i=1}^n \frac{\tilde{\mu}_i}{T} \mathbf{J}_i \right) + \sigma \quad (\text{A.4})$$

Under the local equilibrium hypothesis, the Gibbs relation applies within each infinitesimal element and, in terms of specific properties, is given by:

$$T ds = du + P dv - \sum_{i=1}^n \tilde{\mu}_i dw_i \quad (\text{A.5})$$

where s is the specific entropy, u is the specific internal energy, $v = \rho^{-1}$ is the specific volume, and w_i is the mass fraction of component i .

Multiplying by ρ and applying the material derivative:

$$\rho T \frac{ds}{dt} = \rho \frac{du}{dt} + \rho P \frac{dv}{dt} - \sum_{i=1}^n \mu_i \rho \frac{dw_i}{dt} \quad (\text{A.6})$$

Rearranging gives:

$$\rho \frac{ds}{dt} = \frac{1}{T} \left[\rho \frac{du}{dt} + \rho P \frac{dv}{dt} - \sum_{i=1}^n \tilde{\mu}_i \left(\rho \frac{dw_i}{dt} \right) \right] \quad (\text{A.7})$$

The local energy and species balance equations follow the classical formulation of non-equilibrium thermodynamics as presented in DE GROOT and MAZUR (1984):

$$\rho \frac{du}{dt} = -\nabla \cdot \mathbf{J}_q - P(\nabla \cdot \mathbf{v}) - \mathbf{\Pi} : \nabla \mathbf{v} + \sum_{i=1}^n \mathbf{J}_i \cdot \mathbf{F}_i \quad (\text{A.8})$$

$$\rho \frac{dw_i}{dt} = -\nabla \cdot \mathbf{J}_i + \sum_{r=1}^R \nu_{i,r} \dot{\xi}_r \quad (\text{A.9})$$

where $\mathbf{\Pi}$ is the viscous stress tensor, $\nabla \mathbf{v}$ is the velocity gradient tensor, \mathbf{F}_i is the external force per unit mass acting on species i (such as gravitational or electrical), $\nu_{i,r}$ is the stoichiometric coefficient of species i in reaction r , $\dot{\xi}_r$ is the rate of progress of reaction r , and R is the total number of chemical reactions.

Substituting the energy and species balances (Equation A.8 and Equation A.9) into the entropy rate equation (Equation A.7), yields:

$$\rho \frac{ds}{dt} = \frac{1}{T} \left[-\nabla \cdot \mathbf{J}_q - P(\nabla \cdot \mathbf{v}) - \mathbf{\Pi} : \nabla \mathbf{v} + \sum_{i=1}^n \mathbf{J}_i \cdot \mathbf{F}_i + \rho P \frac{dv}{dt} - \sum_{i=1}^n \tilde{\mu}_i \left(-\nabla \cdot \mathbf{J}_i + \sum_{r=1}^R \nu_{i,r} \dot{\xi}_r \right) \right] \quad (\text{A.10})$$

From the continuity equation, it follows that:

$$\frac{d\rho}{dt} = -\rho(\nabla \cdot \mathbf{v}) \quad (\text{A.11})$$

$$-\frac{1}{\rho} \frac{d\rho}{dt} = \nabla \cdot \mathbf{v} \quad (\text{A.12})$$

$$\rho \frac{dv}{dt} = \nabla \cdot \mathbf{v} \quad (\text{A.13})$$

$$\rho P \frac{dv}{dt} = P(\nabla \cdot \mathbf{v}) \quad (\text{A.14})$$

which cancels the pressure terms in Equation A.10. The entropy equation reduces

to:

$$\begin{aligned}
\rho \frac{ds}{dt} &= -\frac{1}{T}(\nabla \cdot \mathbf{J}_q) - \frac{1}{T}(\mathbf{\Pi} : \nabla \mathbf{v}) \\
&\quad + \frac{1}{T} \sum_{i=1}^n \mathbf{J}_i \cdot \mathbf{F}_i + \frac{1}{T} \sum_{i=1}^n (\tilde{\mu}_i \nabla \cdot \mathbf{J}_i) \\
&\quad - \frac{1}{T} \sum_{r=1}^R \left(\sum_{i=1}^n \tilde{\mu}_i \nu_{i,r} \right) \dot{\xi}_r
\end{aligned} \tag{A.15}$$

Substituting Equation A.15 into: Equation A.4, the entropy balance equation becomes:

$$\begin{aligned}
-\nabla \cdot \left(\frac{\mathbf{J}_q}{T} - \sum_{i=1}^n \frac{\tilde{\mu}_i}{T} \mathbf{J}_i \right) + \sigma &= -\frac{1}{T}(\nabla \cdot \mathbf{J}_q) - \frac{1}{T}(\mathbf{\Pi} : \nabla \mathbf{v}) + \frac{1}{T} \sum_{i=1}^n \mathbf{J}_i \cdot \mathbf{F}_i \\
&\quad + \frac{1}{T} \sum_{i=1}^n (\tilde{\mu}_i \nabla \cdot \mathbf{J}_i) - \frac{1}{T} \sum_{r=1}^R \left(\sum_{i=1}^n \tilde{\mu}_i \nu_{i,r} \right) \dot{\xi}_r
\end{aligned} \tag{A.16}$$

The divergence terms are expanded using the product rule:

$$\frac{1}{T} \nabla \cdot \mathbf{J}_q = \nabla \cdot \left(\frac{\mathbf{J}_q}{T} \right) - \mathbf{J}_q \cdot \nabla \left(\frac{1}{T} \right) \tag{A.17}$$

$$\nabla \left(\frac{1}{T} \right) = -\frac{1}{T^2} \nabla T \tag{A.18}$$

$$\sum_{i=1}^n \frac{\tilde{\mu}_i}{T} \nabla \cdot \mathbf{J}_i = \nabla \cdot \left(\sum_{i=1}^n \frac{\tilde{\mu}_i}{T} \mathbf{J}_i \right) - \sum_{i=1}^n \mathbf{J}_i \cdot \nabla \left(\frac{\tilde{\mu}_i}{T} \right) \tag{A.19}$$

After substituting these identities into the previous expression, the divergence terms cancel out, leaving only contributions associated with gradients and irreversible processes:

$$\sigma = -\frac{\mathbf{J}_q}{T^2} \cdot \nabla T - \frac{1}{T}(\mathbf{\Pi} : \nabla \mathbf{v}) - \sum_{i=1}^n \mathbf{J}_i \cdot \left[\nabla \left(\frac{\tilde{\mu}_i}{T} \right) - \frac{\mathbf{F}_i}{T} \right] + \frac{1}{T} \sum_{r=1}^R \mathcal{A}_r \dot{\xi}_r \tag{A.20}$$

where \mathcal{A}_r is the chemical affinity:

$$\mathcal{A}_r = - \sum_{i=1}^n \tilde{\mu}_i \nu_{i,r} \tag{A.21}$$

and \mathbf{F}_i is the gravitational acceleration g when gravity is the only external field.

Expanding the chemical potential term:

$$\nabla \left(\frac{\tilde{\mu}_i}{T} \right) = \frac{1}{T} \nabla_T(\tilde{\mu}_i) - \frac{h_i}{T^2} \nabla T \quad (\text{A.22})$$

where h_i is the partial enthalpy of component i .

Equation A.20 can be written as:

$$\begin{aligned} \sigma = & -\frac{\mathbf{J}_q}{T^2} \cdot \nabla T - \frac{1}{T} (\boldsymbol{\Pi} : \nabla \mathbf{v}) - \sum_{i=1}^n \mathbf{J}_i \cdot \frac{1}{T} \nabla_T(\tilde{\mu}_i) + \\ & \sum_{i=1}^n \mathbf{J}_i \cdot \frac{h_i}{T^2} \nabla T + \sum_{i=1}^n \mathbf{J}_i \cdot \frac{\mathbf{g}}{T} + \frac{1}{T} \sum_{r=1}^R \mathcal{A}_r \dot{\xi}_r \end{aligned} \quad (\text{A.23})$$

Reorganizing the equation yields the following:

$$\begin{aligned} \sigma = & -\frac{1}{T^2} \left(\mathbf{J}_q - \sum_{i=1}^n \mathbf{J}_i h_i \right) \cdot \nabla T - \frac{1}{T} \sum_{i=1}^n \mathbf{J}_i \cdot [\nabla_T(\tilde{\mu}_i) - \mathbf{g}] \\ & - \frac{1}{T} (\boldsymbol{\Pi} : \nabla \mathbf{v}) + \frac{1}{T} \sum_{r=1}^R \mathcal{A}_r \dot{\xi}_r \end{aligned} \quad (\text{A.24})$$

From Equation A.24 we have:

$$\mathbf{q} = \mathbf{J}_q - \sum_{i=1}^n \mathbf{J}_i h_i \quad (\text{A.25})$$

where \mathbf{q} is the total heat flux and accounts for the conductive heat flux and the diffusion heat flux.

Appendix B

Detailed Derivation of Linear Phenomenological Laws

This appendix provides the detailed derivation of the linear phenomenological laws used in Section 2.8.2, starting from the entropy production expression in Equation 2.36 and applying the constraint $\sum_i \mathbf{J}_i = 0$.

Knowing that:

$$\sum_{i=1}^n \mathbf{J}_i = 0 \quad (\text{B.1})$$

the $n - 1$ independent diffusion fluxes satisfy:

$$\sum_{i=1}^{n-1} \mathbf{J}_i = -\mathbf{J}_n \quad (\text{B.2})$$

Using this relation, the combined contribution of diffusion fluxes to entropy production can be rewritten as:

$$\sum_{i=1}^n \mathbf{J}_i \cdot [\nabla_T(\tilde{\mu}_i) - \mathbf{g}] = \sum_{i=1}^{n-1} \mathbf{J}_i \cdot [\nabla_T(\tilde{\mu}_i) - \mathbf{g}] + \mathbf{J}_n \cdot [\nabla_T(\tilde{\mu}_n) - \mathbf{g}] \quad (\text{B.3})$$

Substituting $\mathbf{J}_n = -\sum_{i=1}^{n-1} \mathbf{J}_i$ gives:

$$\sum_{i=1}^n \mathbf{J}_i \cdot [\nabla_T(\tilde{\mu}_i) - \mathbf{g}] = \sum_{i=1}^{n-1} \mathbf{J}_i \cdot [\nabla_T(\tilde{\mu}_i) - \nabla_T(\tilde{\mu}_n)] \quad (\text{B.4})$$

For a multicomponent petroleum reservoir subject to mass, heat, and gravitational segregation, the phenomenological relations may then be written compactly as:

$$\begin{bmatrix} \mathbf{q} \\ \mathbf{J}_1 \\ \vdots \\ \mathbf{J}_{n-1} \end{bmatrix} = \begin{bmatrix} L_{qq} & L_{q1} & \cdots & L_{q,n-1} \\ L_{1q} & L_{11} & \cdots & L_{1,n-1} \\ \vdots & \vdots & \ddots & \vdots \\ L_{n-1,q} & L_{n-1,1} & \cdots & L_{n-1,n-1} \end{bmatrix} \begin{bmatrix} X_q \\ X_1 \\ \vdots \\ X_{n-1} \end{bmatrix} \quad (\text{B.5})$$

where \mathbf{q} is the total heat flux vector, \mathbf{J}_i is the mass diffusion flux of component i ,

$$X_q = -\frac{\nabla T}{T^2}, \quad X_i = -\frac{1}{T} [\nabla_T(\tilde{\mu}_i) - \nabla_T(\tilde{\mu}_n)],$$

are the corresponding thermodynamic forces.

The explicit expressions for the heat flux and the i -th mass diffusion flux are:

$$\mathbf{q} = -\frac{L_{qq}}{T^2} \nabla T + \sum_{k=1}^{n-1} L_{qk} \left[-\frac{1}{T} \nabla_T(\tilde{\mu}_k - \tilde{\mu}_n) \right] \quad (\text{B.6})$$

$$\mathbf{J}_i = -\frac{L_{iq}}{T^2} \nabla T + \sum_{k=1}^{n-1} L_{ik} \left[-\frac{1}{T} \nabla_T(\tilde{\mu}_k - \tilde{\mu}_n) \right] \quad (\text{B.7})$$

The Curie principle requires that only flux–force pairs with matching tensorial order and symmetry contribute to cross effects. Thus, the terms in Equation B.6 and Equation B.7 represent the allowed couplings between temperature gradients and chemical potential gradients (DE GROOT and MAZUR, 1984).

The heat flux \mathbf{q} contains two contributions, a direct term proportional to ∇T , corresponding to Fourier’s law, and a cross term proportional to $\nabla_T(\tilde{\mu}_k - \tilde{\mu}_n)$, representing the Dufour effect.

For the mass diffusion flux \mathbf{J}_i , the coefficients L_{ik} describe molecular diffusion, while the term proportional to L_{iq} represents the Soret (thermal diffusion) effect (FIROOZABADI, 2016).

Expanding the chemical potential difference in terms of composition and pressure yields:

$$\nabla_T(\tilde{\mu}_k - \tilde{\mu}_n) = \sum_{j=1}^{n-1} \left(\frac{\partial}{\partial x_j} \left(\frac{\mu_k}{M_k} - \frac{\mu_n}{M_n} \right) \right)_{T,P} \nabla x_j + \left(\frac{\partial}{\partial P} \left(\frac{\mu_k}{M_k} - \frac{\mu_n}{M_n} \right) \right)_{T,\mathbf{x}} \nabla P \quad (\text{B.8})$$

Introducing partial molar volumes:

$$\nabla_T(\tilde{\mu}_k - \tilde{\mu}_n) = \sum_{j=1}^{n-1} \left(\frac{1}{M_k} \frac{\partial \mu_k}{\partial x_j} - \frac{1}{M_n} \frac{\partial \mu_n}{\partial x_j} \right)_{T,P} \nabla x_j + \left(\frac{\bar{V}_k}{M_k} - \frac{\bar{V}_n}{M_n} \right) \nabla P \quad (\text{B.9})$$

where \bar{V}_k is the partial molar volume of component k .